THESIS FOR THE DEGREE OF DOCTOR OF PHILOSOPHY

Numerical homogenization of network models and micro-mechanical simulation of paperboard

MORGAN GÖRTZ

Department of Mathematical Sciences
Chalmers University of Technology
Gothenburg, Sweden, 2023

Numerical homogenization of network models and micro-mechanical simulation of paperboard

MORGAN GÖRTZ
ISBN: 978-91-7905-976-7

Doktorsavhandlingar vid Chalmers tekniska högskola
Ny serie nr 5442
ISSN 0346-718X

Department of Mathematical Sciences
Chalmers University of Technology
SE-412 96 Gothenburg, Sweden
Phone: +46 (0)31 772 1000

Fraunhofer-Chalmers Research Centre for Industrial Mathematics
Department of Computational Engineering and Design
Chalmers Science Park
SE-412 88 Gothenburg, Sweden
Phone: +46 (0)31 309 9400
Email: morgan.gortz@fcc.chalmers.se

Printed by Chalmers Reproservice
Gothenburg, Sweden, 2023

Cover: A 4 mm $\times$ 4 mm 400 g/m^2 paperboard model and a synthetic finite element grid with 1 mm $\times$ 1 mm elements.

To my parents who let me find my own path in life.

Abstract

Micro-mechanical simulations of paper products involve complex geometries and challenging numerical problems. This work considers micro-mechanical simulations where individual paper fibers are modeled and resolved. This level of detail is useful in paper-product development, where wood composition and other fiber-based parameters are essential. Several time-dependent and nonlinear micro-mechanical models have been proposed in the literature for accuracy, but these models are limited to small problems.

This work evaluates linear network models as a possible effective tool for paper development, as they permit full commercial-grade paper to be modeled on consumer hardware. This evaluation was performed in the industrial collaboration Innovative Simulation Of Paper (ISOP), with the goal of developing numerically efficient micro-mechanical simulations that are useful for paper product developers. In this work, the linear model was shown to produce accurate results for tensile stiffness, bending stiffness, and tensile strength for paper products with low surface weight. Moreover, accurate tensile stiffness and bending stiffness simulations were possible with commercial-grade three-ply paperboards. Bending stiffness simulations using micro-mechanical models are not well studied, but from this evaluation, it is clear they are now possible on consumer-grade hardware.

Increasing the size of these micro-mechanical models requires specialized numerical techniques that are less resource-intensive. This work developed the theoretical foundation for a finite element-inspired mathematical theory on models based on networks. With this foundation, two resource-efficient methods, an iterative solver and a multiscale method, were mathematically motivated for the discrete network setting. These methods were also validated numerically for the mentioned micro-mechanical paper models. For the iterative approach, bending resistance simulations of models larger than the computational limit of a direct approach were possible.

Keywords: Bending, domain decomposition, local orthogonal decomposition, multiscale, network model, paper model, paper simulation.

List of Papers

This thesis is based on the following publications:

[A] **Morgan Görtz**, Gustav Kettil, Axel Målqvist, Andreas Mark, Fredrik Edelvik, "A numerical multiscale method for fiber networks". Published in WCCM-ECCOMAS 2020 preceedings.

[B] **Morgan Görtz**, Gustav Kettil, Axel Målqvist, Mats Fredlund, Kenneth Wester, Fredrik Edelvik, "Network models for predicting structural properties of paper". Nordic Pulp & Paper Research Journal, vol. 37, no. 4, 2022, pp. 712-724.

[C] **Morgan Görtz**, Fredrik Hellman, Axel Målqvist, "Iterative solution of spatial network models by subspace decomposition". Mathematics of Computation, Vol. 93, 2024, pp. 233–258.

[D] Fredrik Edelvik, **Morgan Görtz**, Fredrik Hellman, Gustav Kettil, Axel Målqvist, "Numerical homogenization of spatial network models". Computer Methods in Applied Mechanics and Engineering, Vol 418, Part B, 2024, 11659.

[E] **Morgan Görtz**, Per Ljung, Axel Målqvist, "Multiscale methods for solving wave equations on spatial networks". Computer Methods in Applied Mechanics and Engineering, Vol. 410, 2023, 116008.

[F] **Morgan Görtz**, Gustav Kettil, Axel Målqvist, Mats Fredlund, Fredrik Edelvik, "Iterative method for large-scale Timoshenko beam models, assessed on commercial-grade paperboard". *Submitted*

Contributions of the author

[A] Görtz developed and implemented the discrete LOD method, implemented compatible versions of the models for the LOD method, performed the numerical experiments, and wrote the manuscript.

[B] Görtz wrote large parts of the implementation of the paper model, researched and analyzed the parameters in the model, performed all of the numerical experiments, and wrote the manuscript.

[C] Görtz worked with the initial theoretical development, supported the theoretical development with numerical insights, implemented and performed the numerical examples in the article, and wrote part of the manuscript.

[D] Görtz worked with the initial theoretical development, supported the theoretical development with numerical insights, implemented and performed the numerical examples in the article, wrote part of the manuscript, and handled the revision.

[E] Görtz supported the theoretical development with numerical insights, developed, implemented, and performed the numerical examples in the article, and wrote the parts with numerical examples in the manuscript.

[F] Görtz wrote large parts of the implementation of the paper model, researched and analyzed the parameters in the model, performed all of the numerical experiments, and wrote the manuscript.

Acknowledgments

I want to thank the Swedish Foundation for Strategic Research (SSF) for supporting my research financially. Parts of this work have been done within the Innovative Simulation Of Paper (ISOP) project, and I would like to thank Mats Fredlund for his insightful comments about everything paper-related. Per Ljung and Fredrik Hellman have been excellent collaborators, and I greatly appreciated working alongside them.

The support of my three supervisors Axel Målqvist, Fredrik Edelvik, and Gustav Kettil has been invaluable. Axel is an excellent educator. His deep understanding of the topics and enthusiasm are contagious. Axel really went above and beyond for me as a supervisor. Fredrik was a great help in developing the overall strategy for this work, and his keen eyes found plenty of embarrassing spelling mistakes in my drafts. During development, plenty of ideas and studies never went anywhere, and some early work did not come to fruition until the very end. Gustav helped me keep on track by narrowing the focus of my work to what was most important.

I want to thank everyone else who supported me when I did not want to work. My very close friends Jessey, Arvid, Anna, and Eva have always been there when I needed to talk to someone. The people I meet at my local dive every Friday are an excellent mix of people, with interesting things always happening. Lastly, I want to thank my family for their company whenever I go back home.

Contents

CHAPTER 1

Introduction

The paper and pulp industries account for 6% of the global industrial energy use and 2% of direct CO_2 emissions [1]. This operation of scale would mean that minor improvements in the process could have substantial effects. These improvements could be using less pulp in products or switching to a pulp with a smaller environmental footprint.

Turning virgin wood into pulp (pulping) is performed mechanically or chemically, producing different fiber types suitable for different applications. The two main types of pulp considered in this work are a thermomechanical pulp (TMP) and a chemothermalmechanical pulp (CTMP). TMP, for example, kraft pulp, produces fine fibers that create sheets with good surface qualities suitable for printing paper. CTMP produces larger fibers that are especially useful for adding bulk to the sheets. The difference between the fibers does not stop at the geometrical properties of the material; they also produce materials with different mechanical properties [2].

Creating a sheet of paper requires numerous steps, resulting in materials with various properties. When forming the paper, the pulp is blended and

mixed with water and additives to form what is known as the stock. This stock can then be used to form raw sheets of paper in a paper machine, which can later be processed by forming, pressing, and drying to form the finished paper product. Analyzing the direct impacts of modifying these steps can be challenging, with the material being complex and modern papermaking machines requiring large amounts of energy and resources.

As mentioned, the analysis of paper-based materials is challenging. The materials are composed of a vast network of fibers, which are connected through mechanical interlocking and hydrogen bonds [3], [4]. Although the problem is complex, there is a long history of evaluating the structural properties of paper by using equations relating the fibers and bonds effect to the mechanical properties of the finished paper [5]–[8]. More recently, continuum models have been used to analyze, for example, paperboard [9]–[11]. These continuum models provide insights into fundamental concepts of how the material acts under load but typically require a wide range of specialized parameters not always accessible to a paper developer in the industry.

Continuum models require effective properties that represent the microstructure. One approach is to find a scale where the material acts as a continuum with a fixed set of effective parameters by finding a representative volume element (RVE) [12], [13] of the material. This approach limits the resolution of the continuum model to the smallest representative scale. Further discretization requires stochastic volume elements (SVE) with stochastic effective properties to be representative [14], [15]. In [15] the effective stochastic properties in an SVE methodology for paper were determined by evaluating micro-mechanical simulations where the individual paper fibers were modeled as beams.

Micro-mechanical models of paper require geometrical and structural properties of the individual cellulose fibers [16]–[19] and an understanding of the fiber-fiber interactions in the material [3], [20], [21]. Early micromechanical simulations evaluated structural properties on sparse network structures [22]–[25] using linear beam models, with recent research analyzing the forming of paper products [26]–[28], and accurate failure mechanics [29]–[32].

In **Paper B**, a micro-mechanical model similar to the Euler–Bernoulli models in [22], [24], but without the rotational dimensions as in [33], was evaluated for larger paper models of low-surface weight (roughly 2/3 the of standard printing paper). Here, it was shown that the models predicted similar structural properties as known paper identities for tensile stiffness, bending stiffness, and tensile strength; moreover, the orthotropic properties were captured. The choice of this simple model, compared to alternatives, was chosen to handle models of larger scales without specialized hardware. **Paper B** acts as a proof of concept for **Paper F**, which has added the Timoshenko components proposed by [25] and extended the numerical validation of tensile stiffness and bending stiffness to commercial-grade paperboard composed of multiple layers of different pulp (5 times the surface weight of standard printing paper). A collaboration with paper product companies Stora Enso and Albany International in the Innovative Simulation Of Paper (ISOP) consortium enabled these numerical results, with the companies providing all experiments needed to set up the models.

The beam models mentioned are based on network models. Network models have been used as the geometry for models in several applications. This type of mathematical object arises when volumes of thin, slender domains are simplified to one-dimensional objects, typically to reduce numerical complexity. This simplification has been evaluated for porous media flow, where the individual pores/cavities in the material are modeled as nodes and the channels between them as the edges of the network model [34]. Other applications are traffic flow, where cities/junctions are the network nodes, and the roads are the edges of the (road) network [35], and heat transfer in [36]. These network problems are usually massive. In particular, evaluating the paperboard models in **Paper F** using a commercial direct linear solver pushed the limit of state-of-the-art consumer-grade hardware (2023). This direct approach was limited to paper models less than 16 mm^3 in size. Going bigger ran into memory limitations, and a less resource-intensive solver was necessary.

When problems become too large to solve using a direct approach (solv-

ing the entire problem at once), you can solve them by dividing the problem into several parts. This may be done by solving smaller problems iteratively that result in subsequently better approximations of the solution to the global problem (iterative method). It could also be performed by splitting the model into parts and defining problems based on some good macro-scale representation of the parts instead of analyzing the complete microstructure at once (multiscale).

A lot of mathematical theory exists for both iterative [37]–[39] and multiscale [40]–[42] approaches for problems posed on continuums; however, less theory exists for problems posed on spatial networks [43]. In both iterative and multiscale approaches, concepts of localization and spread of data are essential. If small local changes in one area lead to large changes somewhere else, splitting the problem into individual parts will be challenging. The method in **Paper C** presents an iterative method for network models based on domain decomposition inspired by [38]. This method is memory efficient, trivially parallelizable, and well-suited for evaluating single systems on large scales. The second method presented in **Paper D**, and used in **Paper E**, is a multiscale method based on the Localized Orthogonal Decomposition method (LOD) [42]. This method is efficient for geometrically linear problems where multiple systems are solved and for models with periodic structures.

Developing the theory for network models was non-trivial, as much of the fundamental theory assumes some continuity and network models are inherently discontinuous. This discontinuity issue was approached by identifying fundamental results required for the continuous counterpart and formulating them for the discrete setting. These identities were proven by formulating three general topological assumptions on the networks: locality, homogeneity, and connectedness, presented in detail in **Paper C**.

This thesis is structured as follows: First, the paper models in **Paper B, F** are presented, along with the results. Then, the topological assumptions on the network in **Paper C** are presented together with a numerical study of the assumptions. This is followed by introducing and presenting the numerical

results of the discrete LOD method evaluated in **Paper A, D, E**. The thesis is then finalized by presenting the domain decomposition method presented in **Paper C**, and how it was used to evaluate the bending stiffness of paperboards with high surface weight using large-scale simulations presented in **Paper F**.

CHAPTER 2

Paper model and structural simulations

2.1 Paper model

Paper-based materials are typically comprised of processed wood, where the cellulose fibers are chemically or mechanically separated (pulping). Pulp, the fibrous material produced from pulping, may have different mechanical properties depending on the wood type and manufacturing process. In micro-mechanical models, these differences are captured by modeling the individual cellulose fibers.

Micro-mechanical simulations of paper are typically resource-intensive, with numerous paper fibers modeled, so simplifications are used to minimize the computational complexity. One such simplification is to treat the fibers as one-dimensional beams, with the volumetric properties imposed analytically. In the models evaluated in this work, each fiber is modeled as multiple beams representing the center of the fiber.

This discretization results in a network where each beam is an edge, and the points connecting the beams are the nodes. Each edge represents a section

of a fiber with specified mechanical properties and cross-section geometry. Paper fibers are hollow, so this geometry includes a cell wall thickness. The hollow part of a paper fiber is called the lumen of the fiber.

Each paper fiber is modeled and placed in a specified domain in a model. The amount of fibers placed depends on the model's surface weight ($\mathrm{kg/m^2}$) and the weight of the individual fibers (coarseness, $\mathrm{kg/m}$). Different methods exist for placing these fibers, ranging from randomized approaches to simulating the paper-forming process. Low surface-weight models were analyzed using random approaches in [44] and **Paper B**; moreover, [44] evaluated the simulation-based approach proposed in [26]. Here, the results presented in **Paper F** are presented, where random network models are evaluated on substantially heavier commercial-grade paperboard.

Experimental data and parameters

Measurement equipment such as L&W's Fiber Tester Plus gives insight into micro-scale information about fibers in various paper pulp. Two pulps are analyzed: an unbleached kraft pulp and a CTMP pulp. Kraft pulps have finer fibers that create good surfaces for printing, whereas CTMP has coarser fibers that are good when bulk is preferable. The geometrical data from two L&W's Fiber Tester Plus scannings are provided in Table 2.1 obtained by Stora Enso in 2020. This data contains the average weight of the fiber (coarseness) and mean geometrical data for five different fiber length intervals. The data is enough to define the fibers' general geometry.

Additional information about the cell wall thickness, cross-section shape, and cross-section area is required for the cross-sections. In the models analyzed, the cell wall thickness was chosen to be 3 μm for all fibers. This cell wall thickness results in some of the fibers being solid (collapsed). For the generated fibers, collapsed fibers have a rectangular cross-section, and non-collapsed fibers are elliptic. The final information required to define the fibers is cross-section area, and that is defined by assuming a constant density of $\rho_f = 1500$ kg/m^3, the density of cellulose, and using the linear relation $A_f = c_f/\rho_f$ where c_f is the coarseness of the fiber. For the two pulps con-

sidered, the kraft fibers have a smaller cross-section area of 131 μm^2, and the CTMP fibers have a cross-section area of 202 μm^2. This larger cross-section area for CTMP produces more non-collapsed fibers, resulting in bulkier fibers as expected.

$$E_s^* = \frac{1}{3}\frac{\rho_s}{\rho_f}\phi E_f, \tag{2.1}$$

where ρ_s, ρ_f are the densities of the sheet and cellulose respectively, E_f is the tensile stiffness of the fiber, $E_s^* = 0.5(E_s^{\mathrm{MD}} + E_s^{\mathrm{CD}})$ is the effective stiffness of the sheet, and E_s^{MD}, E_s^{CD} are the stiffness of the sheet in both principle directions, and ϕ is a constant depending on the average fiber length and the sheet bonds. Using the experimental values from [45] in Table 2.2 and an appropriate ϕ based on the values in [46], the axial Young's modulus for the two pulps is 38 GPa for the fibers in the kraft pulp and 20 GPa for the fibers in the CTMP. The transversal Young's modulus of the fiber is one-third of these values consistent with [19].

Fiber placement

Generating paper models requires a specified length, width, surface weight (g/m^2), and fiber composition. The models presented in this work have multiple layers with different fiber types, where the layers are built in succession on previous layers. For each layer, fibers are created based on the geometrical distribution from pulp experiments (Table 2.2), with the geometry of the fiber taking the shape of a cosine or sine curve between $[0, \pi]$ conforming to the specified shape factor:

$$\text{shape factor} = \frac{\text{length}}{\text{arc length}},$$

The length of a fiber is the diameter of the smallest ball containing the fiber; see Figure 2.1.

This generated fiber is placed randomly in the plane of the sheet with a random rotation.

Table 2.1: Geometrical breakdown of an unbleached kraft pulp and a CTMP pulp, provided by Stora Enso.

Properties	Kraft	CTMP
Coarseness	196 µg/m	303 µg/m
Mean length	2.2 mm	1.7 mm
Mean width	32 µm	36.8 µm
Mean shape factor	86.8%	88%
Length: 0.2-0.5 mm	8.5%	20%
Mean width	22.2 µm	25.4 µm
Mean shape factor	91.4%	88.1%
Length: 0.5-1.5 mm	20.1%	30.2%
Mean width	29.3 µm	35.9 µm
Mean shape factor	88.8%	88.1 %
Length: 1.5-3 mm	45.9%	34.9%
Mean width	32.8 µm	40.9 µm
Mean shape factor	87.1%	89.3 %
Length: 3-4.5 mm	23.5%	13.0%
Mean width	35.6 µm	44.1µm
Mean shape factor	83.7%	85.7 %
Length: 4.5-7.5 mm	2%	1.9%
Mean width	38.3 µm	46.9µm
Mean shape factor	73.6%	78.4 %

Figure 2.1: Illustration of how the length (dotted line) of a fiber (black) is defined.

Table 2.2: Sheet scale experimental data provided in [45] and deduced fiber properties.

Sheet properties [Experiment]	Kraft	CTMP
Grammage	400 g/m^2	400 g/m^2
Density (ρ_s)	770 kg/m^3	423 kg/m^3
Tensile stiff. (E_s^*)	6.4 GPa	1.6 GPa
Fiber Properties [Deduced]		
Cross-section area (A)	131 µm^2	202 µm^2
Axial modulus (E_f)	38 GPa	20 GPa
Transverse modulus (E_f^t)	13 GPa	6.7 GPa
Cell wall thickness	3.0 µm	3.0 µm
Typical cross section	Rectangular	Elliptical

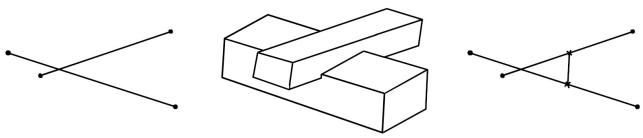

Figure 2.2: Illustration of the bonding process.

Bonding

The connections between the fibers are called bonds. In the network model, bonding between two fibers occurs based on the volumes of the fibers. The volumes analyzed are the edges representing the fiber (using their cross-sectional information). Intersections are found by triangularizing these three-dimensional fiber segments and performing a geometric analysis. If two fiber segments intersect, the bond is placed based on the two points on the edges closest to each other. An illustration of the intersection process is provided in Figure 2.2.

Edges represent the bonds in the network model; each bond can be com-

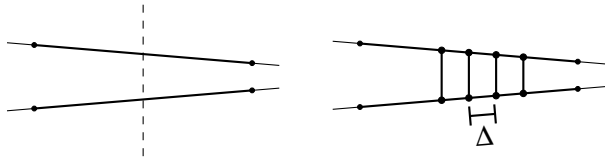

Figure 2.3: Illustration of the edge bond with multiple bonds with a given bond delta (Δ). The left figure shows the two fiber segments before bonding, and the right shows the resulting bond.

posed of multiple bond edges. As mentioned, a bond is placed at the closest points between two intersecting fibers. Moreover, from these two points, more bonds are placed at a fixed distance, bond delta, along the fibers for as long as the two fibers intersect. This propagation results in bonds having different properties based on how connected they are. Figure 2.3 illustrates such bond propagation. The bond delta should be interpreted as a resolution parameter, where the geometries of these bond edges scale appropriately with the bond delta and how connected they are around the bond.

Constitutive models

To analyze the structural properties of a network, a constitutive model is necessary that describes the physical properties of the edges in the network. In [47], an Euler–Bernoulli model was proposed that was derived from a second-order finite difference discretization of classical linear elasticity. This model was developed to be as close as possible to the finite difference model, as a multiscale method similar to the one presented in Chapter 4 works for linear elasticity on continuums. This model was also numerically confirmed to predict tensile stiffness, bending resistance, and tensile strength in **Paper B** along with the orthotropic effects of fiber bias for straight paper fibers.

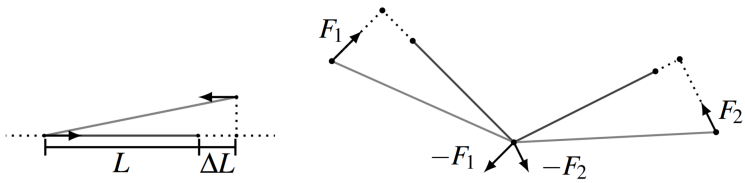

Figure 2.4: The reactionary forces resulting from displacing (gray) edges (black) in the model. The left figure illustrates the forces from edge extension, and the right shows forces from angular deviation.

Euler–Bernoulli

In the Euler–Bernoulli model, the edges representing the paper fibers and bonds are modeled as beams with a linear relation between displacement and reactionary force. The beam model is similar to [22], formalized in [47], and validated for sheets with low surface weight in **Paper B**. This approach is linear and requires the following linear system to be solved:

$$Ku = F,$$

where n is the number of network nodes, $u_i = [u_{i,x}, u_{i,y}, u_{i,z}]$ are the three-directional nodal displacements, $F_i = [F_{i,x}, F_{i,y}, F_{i,z}]$ are the directional applied forces in the i:th network node, and $K \in \mathbb{R}^{3n \times 3n}$ is the connectivity matrix. The connectivity matrix K is comprised of two components: a tensile component (Hooke's) and a bending resistance component (Euler-Bernoulli).

The tensile component is a linearization of Hooke's law for each edge in the network. For each edge, the following force-displacement ratio is used:

$$F = E \cdot A \cdot \varepsilon = \frac{E \cdot A \cdot \Delta L}{L}, \tag{2.2}$$

where F is the magnitude of the resulting force, E is Young's modulus of the edge, A is the cross-section area of the edge, L is the initial length of the edge, and ΔL is a projected length change for linearity. An illustration

of the forces resulting from a displacement can be found in Figure 2.4. The projected length change and resulting force's direction use the initial direction of the edge.

Bending resistance in the model is imposed between two connected edges. This resistance is evaluated in two planes, one plane containing the edge pair (in-plane) and the other orthogonal to the first (out-of-plane). The relation, based on Euler-Bernoulli, is:

$$w''(t) = -\frac{M(t)}{EI} = -\frac{F(L-t)}{EI},$$

where $w(t)$ and $M(t)$ are displacement and the moment at the point t along the deformed edge, EI is Young's modulus times the second moment of area, and L is the length of the edge. At $t = 0$, the center-point of the edge pair, this becomes:

$$w''(0) = -\frac{FL}{E_A I} \Leftrightarrow F = -\frac{E_A I \cdot w''(0)}{L}. \tag{2.3}$$

The $w''(0)$-term in the selected plane in the network model is evaluated using projections (based on normals) and a second-order central difference scheme. With the second derivative in the node between the two edges approximated, the amplitude of the angular deviation forces are calculated by (2.3) and given directions in the plane, normal to the edges (see Figure 2.4).

Timoshenko

Introducing bent fibers led to similar simulation results for tensile stiffness but resulted in too stiff models when bending. This stiffness discrepancy is not an issue when rotational components in a Timoshenko beam model are added. With this more advanced *standard* model, the network model was used to analyze tensile stiffness and bending stiffness of full-scale commercial-grade paperboard in **Paper F**.

The Timoshenko beam model is an extension of the Euler–Bernoulli beam model to handle rotations and shearing. The specific implementation is based on the linear Timoshenko model proposed by [25] for paper materials. In the

linear Timoshenko framework, each node i in the network is described by six degrees of freedom: $[\mathbf{u}^i, \phi^i] = [u_x^i, u_y^i, u_z^i, \phi_x^i, \phi_y^i, \phi_z^i]$, with $\mathbf{u}^i$ representing the displacement and ϕ^i the rotation in the corresponding network node.

The twelve degrees of freedom $(\mathbf{u}^i, \phi^i, \mathbf{u}^j, \phi^j)$ active on an edge (node i and node j), are used to describe a linear relationship to directional forces and moments resulting from the displacement and rotations as follows:

$$K_{ij} \begin{bmatrix} \mathbf{u}^i \\ \phi^i \\ \mathbf{u}^j \\ \phi^j \end{bmatrix} = \begin{bmatrix} \mathbf{F}^i \\ \mathbf{M}^i \\ \mathbf{F}^j \\ \mathbf{M}^j, \end{bmatrix}$$

where $[\mathbf{F}^\star, \mathbf{M}^\star] = [F_x^\star, F_y^\star, F_z^\star, M_x^\star, M_y^\star, M_z^\star]$, for $\star = i, j$.

The linear relation is described in detail in [43], on the following form:

$$K_{ij} = l_{ij} Q_{ij}^T (B_{ij}^T C_{ij} B_{ij}) Q_{ij},$$

where l_{ij} is the length of the edge, $Q_{ij} \in \mathbb{R}^{12\times12}$ is an orthogonal matrix mapping the edge's initial direction to a reference configuration, $B_{ij} \in \mathbb{R}^{6\times12}$ contains the structure of the relation and the length of the edge, and $C_{ij} \in \mathbb{R}^{6\times6}$ is a diagonal matrix with the beam's structural parameters ($[E_f A^{ij}$,$kG_f A^{ij}$,$kG_t A^{ij}$, $G_f I_x^{ij}$,$E_f^t I_y^{ij}$,$E_f^t I_z^{ij}]$). The parameters are as follows: E_f, E_f^t are the elastic modulus of the beam in the axial and transverse direction, (A^{ij}) the cross-section area, $(I^{ij})_\star$ are the second moment of areas, and k is the shear correction factor. The areas are calculated based on the cross-section geometry of the fibers, and k is chosen based on Cowpler selection for either circular or rectangular cross-sections based on whether the fiber is collapsed with Poisson's ratio of 1/3. The shear modulus is set to $G = 3E/8$ with associated Young's modulus E.

Taking the sum of these components results in a system with stiffness matrix K:

$$
\begin{aligned}
K\begin{bmatrix}\mathbf{u}\\ \phi\end{bmatrix} &= \begin{bmatrix}\mathbf{F}\\ \mathbf{M}\end{bmatrix},\\
\mathbf{u} = [\mathbf{u}^1, \mathbf{u}^2, \ldots, \mathbf{u}^n]^T,\ \mathbf{F} &= [\mathbf{F}_1, \mathbf{F}_2, \ldots, \mathbf{F}_n]^T,\\
\phi = [\phi^1, \phi^2, \ldots, \phi^n]^T,\ \mathbf{M} &= [\mathbf{M}_1, \mathbf{M}_2, \ldots, \mathbf{M}_n]^T,
\end{aligned}
\tag{2.4}
$$

The stiffness matrix, K, can then be used to construct linear systems with explicitly imposed boundary conditions to analyze various structural properties.

2.2 Structural simulations

In **Paper B**, various papers of low surface weight (55 g/m^2) were evaluated and validated for tensile stiffness, tensile strength, and bending resistance. Here, the focus will be on the tensile stiffness and bending stiffness results presented in **Paper F** on several commercial-grade three-ply paperboards that are approximately four times (200 g/m^2) and eight times (400 g/m^2) heavier in surface weight. Moreover, an Euler-Bernoulli model was used with straight paper fibers in **Paper B**, and here, models are generated with curved fibers paired with the Timoshenko model. The paperboards considered are based on the experiments performed in [45], but with half the surface weight (200 g/m^2). Bending stiffness simulations on the full surface weight required a different approach than using an off-the-shelf linear solver; these results are presented in Chapter 5.

Paperboard model

Several 200 g/m^2 three-ply paperboards are evaluated using the Timoshenko beam model. These models are composed of three layers, see Figure 2.5, with two surface layers composed of kraft pulp and a bulk layer composed of CTMP. The amount of fibers placed in each layer is determined by a weight

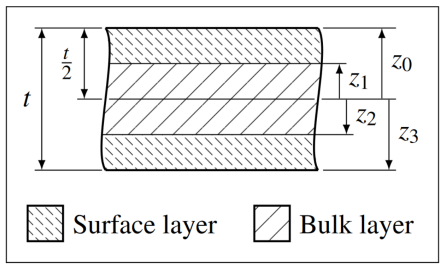

Figure 2.5: An overview of the three-ply paperboards considered in this work, along with ply coordinates z_k and thickness t.

fraction, where 0% means the entire paperboard model is CTMP, and 100% means the entire paperboard model is composed of Kraft pulp. These models are generated using randomization on the specified domains based on the density measurements in Table 2.2, where fibers can cross the layer boundaries (out-of-plane rotation) between individual layers.

Tensile stiffness

When evaluating the tensile stiffness of a model, the model is clamped on two opposite sides and displaced to introduce stress. The models considered are 4 mm $\times$ 4 mm and strained 0.5%. The associated linear system (2.4) is then constructed and solved with the mentioned boundary conditions imposed explicitly. From this solution, the resulting forces can be evaluated to obtain the predicted tensile stiffness. Figure 2.6 illustrates the stresses on individual fibers from one of these simulations.

The tensile stiffness simulation is performed on 11 paperboard models ranging from 0% weight fraction to 100% weight fraction. These results are compared to the theoretical tensile stiffness based on experimental tensile stiffness in Table 2.2 and the theoretical scaling from the associated rule of mixtures (2.5):

$$E_{\text{Sheet}} = E_{\text{CTMP}} \frac{t_{\text{CTMP}}}{t} + E_{\text{kraft}} \frac{t_{\text{kraft}}}{t}. \tag{2.5}$$

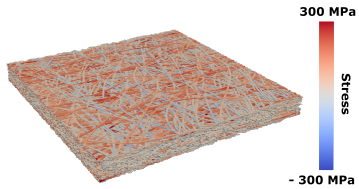

Figure 2.6: An illustration of the solution of a tensile stiffness simulation.

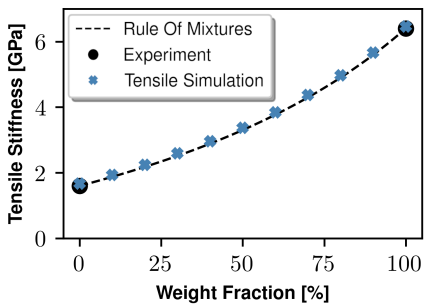

Figure 2.7: Tensile stiffness for different weight distributions in various 200 g/m^2 three-ply paperboard. The black circular markers are experimental measurements, the colored cross markers are simulated results, and the dashed lines are the rule of mixtures based on the experimental tensile stiffness in [45] of sheets made from one pulp.

Figure 2.7 presents the simulation results and shows that the model is consistent with the theoretical scaling.

Bending stiffness

Bending stiffness for paper products such as paper and paperboard is normalized using Euler–Bernoulli theory. This means that shear effects are not considered, and sufficiently long bending levers are required for comparable results. In [48], the recommended lever-to-thickness ratio is over 40, and with the thickest 200g/m^2 paperboard considered, this would mean a lever of

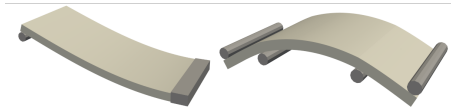

Figure 2.8: Illustrations of the two and four-point bending stiffness experiments.

at least 19 mm is suggested.

Here, two bending stiffness experiments are simulated: the two-point and four-point methods. The experimental results in [45] were obtained using a two-point method, whereas, for thicker materials with greater anisotropic shear properties, the four-point method is preferable. Figure 2.8 illustrates the two-point and four-point bending stiffness methods.

Two-point simulation

The experiments performed in [45] for the bending stiffness was a two-point method. This approach has one side of the paper sample clamped with the opposite side displaced a specified distance out-of-plane. The probe performing the displacement also measures the resulting force. In the simulation, one side of the model is clamped, and the other is displaced with only the z-coordinate locked.

For the bending stiffness simulations, the models have a width of 4 mm, as in the tensile simulations, but have different bending levers (length). The simulations are performed by constructing and solving the associate linear system, and then the bending stiffness is evaluated as [48]:

$$S_b = \frac{F^b l_b^3}{3\delta_b 0.004}, \tag{2.6}$$

where F^b is the sum of lateral forces resulting from the displacement and l_b, δ_b are the leaver and displacement in the two-point method.

Four-point simulation

In the four-point bending stiffness experiment, shearing effects are negated by not clamping the sample. This is done by displacing the paper at four points along the lever and evaluating the displacement and force when bent. In the simulation, five planes are considered perpendicular to the bending lever. These five planes are at the start and end of the paperboard model, the midpoint, and 25% and 75% along the bending lever from the start. At the start and end of the model, Dirichlet conditions are placed only in out-of-plane displacement to a specified lateral displacement. The model has similar out-of-plane displacement Dirichlet conditions at the 25% and 75% planes of interest, whereas here, they are fixed at zero. The final plane at the model's center has zero in-plane Dirichlet conditions for the displacement to make the system solvable. Note that no Dirichlet conditions are placed on the rotational degrees of freedom.

The bending stiffness is then calculated by [48]:

$$S_b = \frac{\bar{F}^b(0.2l)(0.8)^2}{8\delta_b 0.004}, \tag{2.7}$$

where $\bar{F}^b$ is the average size of the four out-of-plane forces acting on the four planes with out-of-plane Dirichlet conditions, l_b is the length of the lever, and δ_b is the average out-of-plane displacement in the center plane with in-plane Dirichlet conditions.

Bending lever domain study

The two-point and four-point methods are simulated for multiple levers to compare the shear effects of small bending levers. Figure 2.9 presents the bending stiffness results evaluated for the thickest paperboards composed entirely of CTMP. These results are compared to the theoretical bending stiffness computed using a straight Timoshenko beam representing the entire sheet. The Youngs modulus of this sheet is the experimental tensile stiffness in Table 2.2 with various Elastic–Shear modulus ratios (E/G). These ratios

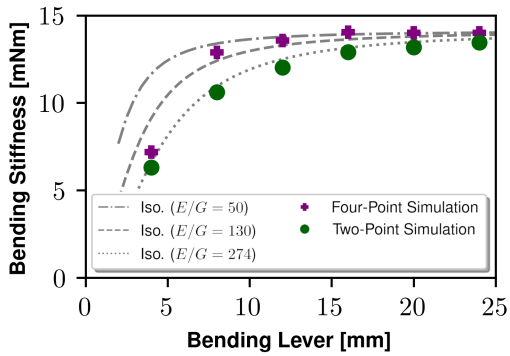

Figure 2.9: Results from two-point and four-point bending stiffness simulations for different bending levers for 200 $\mathrm{g/m^2}$ paperboard composed entirely of CTMP. The dashed line is a prediction based on the experimental tensile stiffness of the sheet using a Timoshenko beam representation of the paper sheet.

are taken from the literature: 50 [48], 130 [49], and 274 [50]. From the study in Figure 2.9, the two-point simulation anticipates a shear ratio on the higher end with a slightly different scaling. The difference in scaling is discussed in [48], where boundary effects around the clamp could explain the discrepancy. For the four-point method, some shear effects are visible, which might have been introduced in the simplifications made when imposing the boundary conditions. With that in mind, this domain study indicates that at least a 16 mm bending lever should be simulated for the four-point method, and a 24 mm should be used for the two-point method. Thus allowing for shorter bending levers when evaluating bending stiffness if the four-point method is used.

Multi-laminar bending stiffness

The theoretical scaling of bending stiffness for n-ply paperboard is presented in [45], as follows:

$$S_b = D - \frac{B^2}{A}, \tag{2.8}$$

$$A = \sum_{k=1}^{n} (E_x)_k (z_k - z_{k-1}),$$

$$B = \frac{1}{2} \sum_{k=1}^{n} (E_x)_k (z_k^2 - z_{k-1}^2),$$

$$D = \frac{1}{3} \sum_{k=1}^{n} (E_x)_k (z_k^3 - z_{k-1}^3),$$

where $(E_x)_k$ is the tensile stiffness of the k:th ply and the ply-coordinates, z_k, are defined as:

$$z_k = \begin{cases} -t/2, \ k = 0, \\ z_{k-1} + t_k, \ \text{else}, \end{cases}$$

where t is the thickness of the paperboard and t_k is the thickness of the k:th ply. Figure 2.5 presents the associated coordinates needed to compute the bending stiffness.

This theoretical bending stiffness is compared to the eleven 200 g/m^2 three-ply paperboards considered in the tensile stiffness simulation. The two- and four-point methods are used to evaluate the bending stiffness with the bending levers from the domain study (24 mm and 16 mm). Figure 2.10 presents the result of this study and shows that both the two-point and four-point simulations can predict the quadratic theoretical scaling proposed in (2.8) using the experimental values in Table 2.2.

Computational requirements

These simulations are resource intensive, with the numerical metrics of the four-point bending resistance simulations in Figure 2.10 presented in Ta-

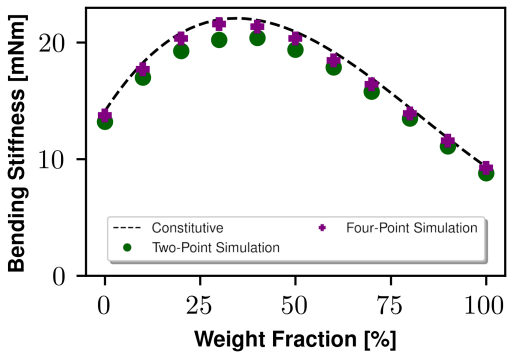

Figure 2.10: Bending stiffness for different weight distributions in various 200 g/m^2 three-ply paperboard. The colored markers are simulated results, and the dashed line is calculated using multi-laminar theory based on experimental results [45].

Table 2.3: Numerical metrics for solving three four-point bending stiffness simulations in Figure 2.10.

Weight Fraction	0 %	50 %	100 %
Nodes (10^6)	2.12	2.95	3.77
Beams (10^6)	2.9	4.1	5.3
System dim. (10^6)	12.7	17.7	22.6
Memory (RAM)	44.8 Gb	54.1 Gb	90.3 Gb
Wall-clock	12.5 min	19 min	35 min

ble 2.3. The results illustrate the size of network problems that can be solved with today's (2023) consumer-grade hardware (AMD Ryzen 9 3900X 12-Core, 128 GB RAM). The main issue with scaling this approach further is the memory limitation. Generating the network models is not an issue, requiring only a small part of the memory during the simulation. The limitation occurs when solving the linear system using a direct solver.

In Chapter 4 and 5, alternative approaches to evaluating these network problems are proposed. The theory and development of these alternative methods to direct solvers are motivated as approaches are limited [43]. The rest of this thesis will present the theoretical framework used to develop these methods and will end by performing the bending stiffness simulations on the full surface weight (400 g/m^2) paperboards in [45]

CHAPTER 3

Network theory and problem formulation

In this Chapter, the mathematical definition of a network is presented, along with assumptions on the structure of the network required to formulate the theoretical results in **Paper C, D, E**, and numerical evaluations of these assumptions. Then, the model problems posed on these networks are described. Finally, a partition of the network is presented, along with a function to define neighborhoods on this scale, and a lower-dimensional discrete function space with an accompanying interpolant.

3.1 Theoretical foundation

Before anything else, we first define what a spatial network is.

Definition 1 (Spatial network)**:** *A spatial network, $\mathcal{G} = (\mathcal{N}, \mathcal{E})$, is defined by an indexed node set $\mathcal{N} = \{x_1, x_2, \ldots x_n\}$, $x_i \in \mathbb{R}^d$, and an edge set $\mathcal{E} \subset \{\{x_i,\ x_j\} :\ x_i, x_j \in \mathcal{N}$ and $x_i \neq x_j\}$, where d is the spatial dimension of the network. An element in the nodal set $\mathcal{N}$ is called a node and these nodes are*

connected by edges that are defined by the unordered pairs in the edge set $\mathcal{E}$. The notation $i \sim j$ is used to say that $\{x_i, x_j\} \in \mathcal{E}$.

A network is a discrete geometrical object with defined paths between points. This space requires special consideration when talking about the distance between two nodes. Here, we assume that an edge between the points x_i and x_j represents a straight line segment and define the length of an edge by the regular Euclidian norm:

Definition 2 (Edge length)**:** *The length of an edge, $\{x_i, x_j\} \in \mathcal{E}$, in a spatial network is defined by the Euclidian distance, $|x_i - x_j|$, between the two nodes in the node pair.*

This "edge length" gives us the distance between two network nodes connected by an edge. To generalize this notion of distance to nodes connected by transversing several edges, we first define the notion of a path.

Definition 3 (Path)**:** *The sequence of nodes, $\{z_k\}_{k=1}^m$, is called a path from x_i to x_j if $x_i = z_1 \sim z_2$, $z_2 \sim z_3$, …, $z_{m-1} \sim z_m = x_j$.*

Assuming there exists a path between two nodes, one concept of distance between two nodes would be the shortest path, where the length of the path is the length of the edges comprising it, i.e.:

$$d_p(x_i, x_j) = \min_{\{z_k\}_{k=1}^m \text{ path from } x_i \text{ to } x_j} \sum_{i=1}^{m-1} |z_i - z_{i+1}|$$

This concept of distance on a graph forms a metric space assuming edges have non-zero length and that at least one path always exists between two points, i.e. the network is connected:

Definition 4 (Connected Network)**:** *A spatial network $\mathcal{G} = (\mathcal{N}, \mathcal{E})$ is connected if for any two distinct nodes $x_i, x_j \in \mathcal{N}$, there exists a path between them.*

With this fundamental notation, we can form our first set of restrictions on the networks considered:

Assumption 1:

- *The nodes in the nodal set reside in some hyperbox* $\Omega = [0, s_k]^d$ *with side lengths* $s_k > 0, k = 1, \ldots, d$.
- *Every edge in the network has a non-zero length.*
- *The network is connected*

With the first set of assumptions, we can define the discrete function space $\hat{V}$ as the set of real-valued functions defined for each node in $\mathcal{N}$. Note that the spatial network considered induces this space. In this space, we define the regular l_2 inner product as:

Definition 5 (l_2 operator)**:**

$$(u, v) = \sum_{x_i \in \mathcal{N}} (u(x_i), v(x_i)), \quad u, v \in \hat{V}.$$

Two important linear operators are defined using this inner product and function space $\hat{V}$. First $M : \hat{V} \to \hat{V}$, which is the following weighted l_2 scalar product:

Definition 6 (M operator)**:**

$$(Mu, v) = \sum_{x_i \in \mathcal{N}} (M_i u, v), \quad (M_i u, v) = \frac{1}{2} \sum_{i \sim j} |x_i - x_j| u(x_i) v(x_i),$$

where $\sum_{i \sim j}$ is short hand for the sum of all edges $\{x_i, x_j\} \in \mathcal{E}$. The second operator is $L : \hat{V} \to \hat{V}$, which acts as a differential operator:

Definition 7 (L operator)**:**

$$(Lu, v) = \sum_{x_i \in \mathcal{N}} (L_i u, v), \quad (L_i u, v) = \frac{1}{2} \sum_{i \sim j} \frac{(u(x_i) - u(x_j))(v(x_i) - v(x_j))}{|x_i - x_j|}.$$

From these two definitions, we can derive the M-norm: $|u|_M^2 = (Mu, u)$,

and the L semi-norm $|u|_L^2 = (Lu, u)$.

The M-operator can be interpreted as an L_2-type scalar product over all the edges in the network:

$$\sum_{\{x_i,x_j\}\in\mathcal{E}} \int_{x_i}^{x_j} uv\, dx \approx \text{[Trapezoidal rule]}$$

$$\approx \frac{1}{2} \sum_{\{x_i,x_j\}\in\mathcal{E}} |x_i - x_j| \left(u(x_i)v(x_i) + u(x_j)v(x_j)\right)$$

$$= \frac{1}{2} \sum_{x_i\in\mathcal{N}} \sum_{i\sim j} |x_i - x_j| u(x_i)v(x_i) = (Mu, v).$$

In particular, $|1|_M^2$ is the total length of all edges in the network.

The L operator can similarly be interpreted as a L_2-type scalar product of edge directional derivatives over all edges:

$$\sum_{\{x_i,x_j\}\in\mathcal{E}} \int_{x_i}^{x_j} (\nabla u \cdot \partial_{ij})(\nabla v \cdot \partial_{ij}) dx \quad \left[\, \partial_{ij} = \frac{x_j - x_i}{|x_j - x_i|} \right]$$

$$\approx \sum_{\{x_i,x_j\}\in\mathcal{E}} \int_{x_i}^{x_j} \left(\frac{u(x_j) - u(x_i)}{|x_j - x_i|}\right) \left(\frac{v(x_j) - v(x_i)}{|x_j - x_i|}\right) dx$$

$$= \sum_{\{x_i,x_j\}\in\mathcal{E}} |x_j - x_i| \left(\frac{u(x_j) - u(x_i)}{|x_j - x_i|}\right) \left(\frac{v(x_j) - v(x_i)}{|x_j - x_i|}\right)$$

$$= \sum_{\{x_i,x_j\}\in\mathcal{E}} \left(\frac{(u(x_j) - u(x_i))(v(x_j) - v(x_i))}{|x_j - x_i|}\right)$$

$$= \frac{1}{2} \sum_{x_i\in\mathcal{N}} \sum_{i\sim j} \frac{(u(x_j) - u(x_i))(v(x_j) - v(x_i))}{|x_j - x_i|} = (Lu, v)$$

An important property of the L operator is that it has a one-dimensional kernel if the network is connected, with the eigenspace of this kernel being the constant functions: $|u|_L = 0 \Leftrightarrow$ u constant.

Remark: For equidistant grids with side length h, this L operator is the matrix obtained by the second-order finite difference discretization of the Laplacian multiplied by h.

These discrete operators M and L will be used similarly as the L_2 inner-product and H_1 semi-inner-product respectively. With that in mind, local versions of the operators are necessary, and for compactness, the set function N is defined that maps a set in $\mathbb{R}^d$ to the node indices.

Definition 8:

$$N(\omega) = \left\{x_i \in \mathcal{N},\ x_i \in \omega\right\}.$$

With the set function, we define $(M_\omega u, v) = \sum_{i \in N(\omega)} (M_i u, v)$, $|u|^2_{M(\omega)} = (M_\omega u, u)$, where the local counterparts of L are defined analogously.

In the numerical examples in this work, vector-valued problems will be considered. In particular, the Euler-Bernoulli model is three-dimensional, and the Timoshenko beam model is six-dimensional. To handle the vector-valued case, we introduce the product space

$$\hat{\mathbf{V}} = \hat{V}^{d_s},$$

where d_s is the dimension of the data for each node. Note that the solution dimension does not have to coincide with the geometric dimension of the problem.

An object of $\mathbf{v} \in \mathbf{V}$ is written component-wise $\mathbf{v} = [v_{(1)}, \ldots, v_{(d_s)}]$. Moreover, vector valued versions of L and M are defined as:

$$\begin{aligned} \mathbf{M}_i \mathbf{v} &= [M_i v_{(1)}, \ldots, M_i v_{(d_s)}] \\ \mathbf{L}_i \mathbf{v} &= [L_i v_{(1)}, \ldots, L_i v_{(d_s)}], \end{aligned} \tag{3.1}$$

$$|\mathbf{v}|^2_{\mathbf{M}} = (\mathbf{M}\mathbf{v}, \mathbf{v}),\ \ |\mathbf{v}|^2_{\mathbf{L}} = (\mathbf{L}\mathbf{v}, \mathbf{v}),\ \ (\mathbf{u}, \mathbf{v}) = \sum_{i=1}^{d_s} (u_{(i)}, v_{(i)}), \tag{3.2}$$

with spatial restrictions denoted as in the scalar case.

3.2 Network assumptions

When developing the theoretical framework, it became apparent that some general structural restrictions were required on the networks. In the theory, the spread of information has to be localized geometrically, and three significant problems for this were isolated: long edges spanning the domain, non-sufficient connectedness, and poor network coverage. To understand the first two issues, consider heat diffusing throughout the network from a point source. In the case of long edges, heat could propagate long distances without diffusing locally. With non-sufficient connectedness, the spread of heat between two points geometrically close could require paths throughout the entire domain. The last issue of network coverage is required to guarantee that there are parts of the network where the heat can diffuse.

Words such as *long*, *non-sufficient*, and *poor* do not say much without some sense of scale. Network models are discrete objects, and at some ε scale, every network edge becomes *long*, and any network becomes *non-sufficiently* connected with *poor* coverage. These concepts were quantified in **Paper C** as three assumptions on the structure of the network. These assumptions are based on some smallest distance $R_0 > 0$, representing the smallest scale where the network can be viewed as a homogenous and well-connected structure.

Three main assumptions are imposed on the network. In the case of long edges, it is trivial:

Assumption 2 (locality)**:** *The edge length* $|x_i - x_j| < R_0$ *for all edges* $\{x_i, x_j\} \in \mathcal{E}$.

For the other two, connectivity and even coverage, parts of the network have to be isolated and compared. For this, we introduce the following boxes:

$$B_R(x) = \tilde{B}_R(x) \cup (\overline{\tilde{B}_R(x)} \cap \partial\Omega),\ x \in \Omega$$

$$\tilde{B}_R(x) = [x_1 - R, x_1 + R) \times \cdots \times [x_d - R, x_d + R)$$

The open boundaries of the boxes, B_R, will later be important as they will be used to form a partition of the domain.

Homogeneity

Recall that $|1|^2_M$ represents the total length of all edges in the network. Using this, we may formulate a sense of relative edge coverage between two areas of the network. Given two boxes with the same radius $R > 0$, $B_R(x)$ and $B_R(y)$, centered around two points $x, y \in \mathbb{R}^d$, the ratio:

$$\frac{|1|^2_{M,B_R(x)}}{|1|^2_{M,B_R(y)}}$$

gives a sense of how much more edges-coverage there is in $B_R(x)$ compared to the box $B_R(y)$. This may be generalized further by introducing the notion of edge density: $\text{vol}(B_R(x))^{-1}|1|^2_{B_R(x)}$. This edge density allows for a representative comparison of boxes with different radii. This ratio is used to define the homogeneity assumption.

Assumption 3 (Homogeneity)**:** *For all $R \geq R_0$, there exists a uniformity constant $\sigma \geq 0$:*

$$\max_{B_R(x)\subset\Omega} \frac{|1|^2_{M,B_R(x)}}{vol(B_R(x))} \leq \sigma \min_{B_R(y)\subset\Omega} \frac{|1|^2_{M,B_R(y)}}{vol(B_R(y))}$$

Connectivity

The final assumption to guarantee connectivity is formulated as follows. Take all the edges with a node in the box $B_R(x)$, and create a new network composed of those edges. In general, this results in the smaller network being non-connected. The concept of connectivity can then be quantified by how much further out you must go in the original network to find paths to connect the smaller network. For the network to be considered well connected with respect to the length scale R_0, we assume it won't be further than $B_{R+R_0}(x)$. This is formulated as follows, with an illustration of the assumption presented in Figure 3.1.

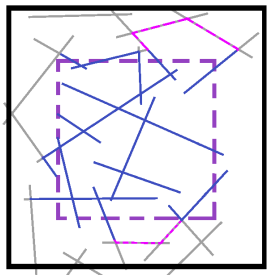

Figure 3.1: Illustration of Assumption 4. The dashed box represents B_R, the black box represents B_{R+R_0}, and the rest are different parts of the network $\mathcal{G}$. The blue parts are all the edges with a node in B_R, and the dashed pink edges are the components needed to connect the blue network to create the connected subgraph $\overline{\mathcal{G}}$.

Assumption 4 (Connectivity assumptions)**:** *For any box $B_R(x)$, $R \geq R_0, x \in \Omega$ it is possible to find a connected subgraph $\overline{\mathcal{G}}$ of $\mathcal{G}$ that:*

- *contains all edges with one or more endpoints in the box $B_R(x)$*
- *only use components from $\mathcal{G}$ contained in the box $B_{R+R_0}(x)$*

An interesting—and useful—consequence of the connectivity assumption is that it is possible to formulate Friedrichs and Poincaré inequalities between the linear operators M and L.

Lemma 1 (Friedrich and Poincaré inequalities)**:** *If Assumption 4 holds, then there exists a $\mu > 0$ such that for all $R \geq R_0$ and $x \in \Omega$:*

- *(Friedrichs) If $B_R(x)$ contains a node $x \in \mathcal{N}$ of which $V = \{v \in \hat{V} : v(x) = 0\}$ then:*

$$|v|_{M,B_R(x)} \leq \mu R |v|_{L,B_R+R_0},$$

  for all $v \in V$.
- *(Poincaré) If $B_R(x) \subset \Omega$:*

$$|v - c|_{M,B_R(x)} \leq \mu R |v|_{L,B_R+R_0},$$

  where $c = c(R,x,v)$ is some constant function, for all $v \in \hat{V}$.

The proof of these inequalities is not very technical. It is based on the fact that M is a diagonal operator (with positive diagonal), and L has a one-dimensional kernel (the constant functions) if the network is connected. In essence, consider the box $B_R(x)$ centered around $x \in \mathbb{R}^d$. Then by Assumption 4 we can find a connected subgraph, $\overline{\mathcal{G}}$, with associated linear operators $\overline{M}, \overline{L}$ such that:

$$|v|^2_{M,B_R(x)} \leq |v|^2_{\overline{M}}$$

$$|v|^2_{\overline{L}} \leq |v|^2_{L,B_{R+R_0}(x)}$$

The proof of the Friedrichs inequality is then completed by using that the kernel of $\overline{L}$ has one dimension ($\overline{\mathcal{G}}$ is connected), with the constant functions being the eigenfunctions of the kernel. Note that in the Friedrichs inequality, we assume that the function is zero at a point, which means that the only constant function in V is 0. This gives:

$$0 > \lambda_2 = \min_{v \neq 0} \frac{(\overline{L}v, v)}{(\overline{M}v, v)},$$

using the min-max theorem. With this, we get:

$$|v|^2_{\overline{M}} \leq (\lambda_2)^{-1} |v|^2_{\overline{L}} = R^2((\lambda_2)^{-1}R^{-2})|v|^2_{\overline{L}} = R^2\mu^2|v|^2_{\overline{L}}, \tag{3.3}$$

where $\mu = (\lambda_2)^{-1/2}R^{-1}$ is the constant. For the complete technical proof and the proof of the Poincaré inequality, see **Paper C** Lemma 3.6.

Remark: This constant λ_2 is the second smallest eigenvalue of the operator L, a weighted version of the graph Laplacian matrix. The second smallest eigenvalue of a connected graph's associated graph Laplacian is known as the network's Fiedler number [51], or algebraic connectivity. Grid-type networks have high algebraic connectivity, whereas networks based on space-filling curves, such as Peano's curve, have low algebraic connectivity.

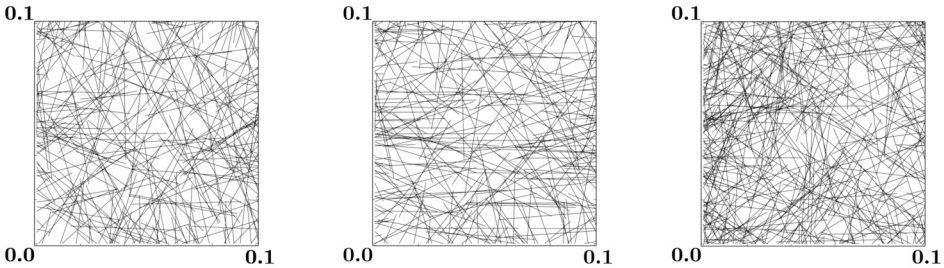

Figure 3.2: The lower left corners ($[0.0, 0.1]^2$) of the three types of fiber networks analyzed. The left network was generated uniformly, the center network has a bias in fiber rotation, and the right network has a bias in fiber placement.

Numerical evaluation

In **Paper C**, the homogeneity and connectivity assumptions were evaluated numerically. In the example, the homogeneity (Assumption 3) and connectivity (Assumption 4) assumptions are visualized by generating and analyzing three types of two-dimensional fiber networks. These networks are generated stochastically using different distributions. The first network is generated uniformly, where fibers are placed and rotated without bias. The second network has a bias in the fiber rotation, and the third has a bias in the fiber placement. Illustrations of the network structures are presented in Figure 3.2.

The networks evaluated were created by placing straight line segments of length $r = 0.005$ in the domain $\Omega = [0,1]^2$ until the total length of all edges in the network was $|1|_M^2 = 1000$. Networks vary by using different stochastic distributions when placing and rotating the fibers. The network is then the line segments, with added nodes at each intersection with any potentially disconnected line segments discarded.

The homogeneity assumption (Assumption 3) can be illustrated by estimating:

$$\sigma = \frac{\max_{B_R(x)\subset\Omega} |1|^2_{M,B_R(x)}}{\min_{B_R(y)\subset\Omega} |1|^2_{M,B_R(y)}},$$

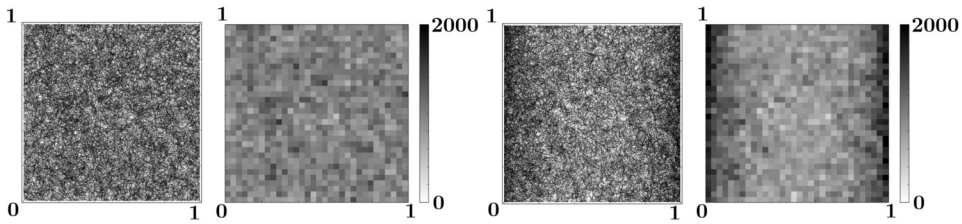

Figure 3.3: Entire networks and illustrations of the homogeneity assumption for the uniform fiber network (left) and the network with more fibers along the lines $x_1 = 0$ and $x_1 = 1$ (right). The boxes represent $(2R)^{-d}|1|^2_{M,B_R(x)}$ for the respective box $B_R(x)$ when $R^{-1} = 64$

for different length scales. This is done by placing a uniform grid over the network and analyzing the density in the boxes. The side lengths analyzed are $R^{-1} = 4$, 8, 16, 32, and 64. This was done for all the three networks. Figure 3.3 illustrates such a grid and evaluations of two of the networks, and Table 3.1 presents the results. We detect an increase in σ as R decreases and larger values for the last example, with bias in fiber placement, as expected.

The connectivity assumption (Assumption 4) is evaluated with respect to the same grids for the analysis of the homogeneity of the network. We know the assumption holds if we can find a connected subgraph $\overline{\mathcal{G}}$, on $B_{R+R_0}(x)$, and the R_0 considered here is $R_0^{-1} = 64$. Finding connected subgraphs was possible in all cases. To quantify how connected these subgraphs were we estimated μ in Lemma 1 by trying to find the smallest connected subgraph for each box in the grid. This connected subgraph, $\overline{G}$, was found using a breadth-first search scheme, resulting in minimal components. The subgraph was then used in (3.3), and the second smallest eigenvalue for the associated problem was found. Figure 3.4 plots λ_2^{-1} with respect to R, and from these figures it is apparent that λ_2^{-1} scales as a constant times R^2. This constant is μ^2 in (3.3) and is presented for all grid sizes in Table 3.1.

Table 3.1 illustrates that the constants σ and μ increase when the scale R decreases. These constants are large when the network is relatively poorly

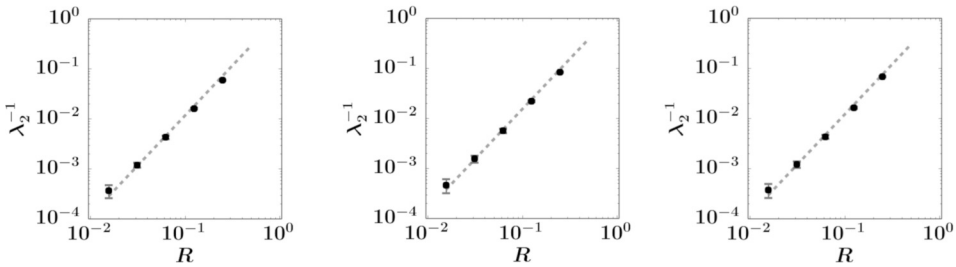

Figure 3.4: The relation between λ_2^{-1} and R for the following networks: uniform (left), fiber orientation bias (center), and fiber placement bias (right). The dots represent the average λ_2^{-1} for the given grid size, the feet the standard deviation, and the dashed lines illustrate R^2 scaling.

Table 3.1: Table with homogeneity constant σ and connectivity constants μ for different R attained numerically

	$R^{-1}=4$	$R^{-1}=8$	$R^{-1}=16$
Uniform	(1.04,0.49)	(1.08,0.53)	(1.27,0.57)
Rand. Orient.	(1.04,0.59)	(1.08,0.61)	(1.27,0.69)
Rand. Domain	(1.04,0.53)	(1.57,0.54)	(2.13,0.58)

	$R^{-1}=32$	$R^{-1}=64$
Uniform	(1.85,0.675)	(3.42,1.53)
Rand. Orient.	(1.87,0.83)	(2.93,1.35)
Rand. Domain	(3.1,0.76)	(6.86,1.45)

connected and inhomogeneous, so this is expected. This increase is most evident for the finest grid size. An interesting result is that the network with bias in the fiber orientation generally has lower connectivity than the network with a uniform distribution but a similar homogeneity constant. In the networks with bias in fiber placement, lower homogeneity is observed as expected, but surprisingly, they have comparable connectivity to the non-biased network.

3.3 Problem formulation

With the assumptions on the network formulated, we now define the type of problems considered. Generally speaking, the problems analyzed are discretizations of elliptic diffusion problems such as heat and linear elasticity on network geometries. The problems are related to a stiffness matrix $K : \hat{V} \to \hat{V}$ for scalar problems and $\mathbf{K} : \hat{\mathbf{V}} \to \hat{\mathbf{V}}$ for vector-valued problems, where $\hat{V}, \hat{\mathbf{V}}$ are all scalar/vector-valued functions defined on the nodes of the network. For the sake of brevity, we will stick to scalar notation. In **Paper E** the framework was extended to hyperbolic problems, but for now, let the problem take the form: Find $\hat{u} \in \hat{V}$ such that:

$$\begin{cases} K\hat{u} = \hat{f}, \\ \hat{u}(x) = g(x),\ x \in \Gamma \end{cases}$$

where $\hat{f},\ g$ is the data, and Γ is part of the boundary of Ω where Dirichlet conditions are imposed. The solution $\hat{u}$ is split into two parts $\hat{u} = u + h$, where h is some function fulfilling the Dirichlet boundary conditions, i.e., $u(\Gamma) = 0$. This transforms the problem into the following homogeneous problem: Find $u \in \hat{V}$:

$$\begin{cases} Ku = f, \\ u(x) = 0,\ x \in \Gamma \end{cases},$$

where $f = \hat{f} - Kh$. To simplify notation further we introduce the solution space $V = \{v \in \hat{V} : v(x) = 0, \forall x \in \Gamma\}$. The final strong form can then be

expressed as:

$$\text{Find } u \in V \ : \ Ku = f. \tag{3.4}$$

Moreover, we define the weak form as:

$$\text{Find } u \in V \ : \ (Ku, v) = (f, v), \ \forall v \in V. \tag{3.5}$$

3.4 Model assumptions

With the structure of K formalized, we introduce the following assumptions on K:

Assumption 5 (Model assumption)**:**

1. *K is bounded and coercive on V with respect to L, i.e. there are constants $\alpha > 0$ and $\beta < \infty$ such that*

$$\alpha(Lv, v) \leq (Kv, v) \leq \beta(Lv, v) \tag{3.6}$$

   for all $v \in V$,
2. *K is symmetric, $(Kv, w) = (Kw, v)$.*

Where the first assumption will guarantee that the operator K is spectrally equivalent to the operator L, and the second is to guarantee that the problem is symmetric.

The existence of network nodes on the boundary set is important for the existence and uniqueness of the solution to (3.5). Moreover, for some of the theory it is required that it is possible to find Dirichlet nodes at the R_0 length scale introduced in Chapter 3. This requirement is formalized as follows:

Assumption 6 (Boundary density assumption)**:** *For any $y \in \Gamma$, there is an $x \in \mathcal{N}(\Gamma)$ such that $|x - y| < R_0$.*

This assumption guarantees that a box, $B_{R_0}(x) \subset \Omega$, $x \in \Omega$, containing part of a Dirichlet boundary will contain at least one Dirichlet node. Moreover, it also means that there exist points on the boundary (in any meaningful setting)

making $(u,v)_K$ coercive, a scalar product, and $(u,u)_K = |u|_K^2$ a norm on V.

Definition 9 (K scalar-product and norm)**:**

$$(u,v)_K := (Ku,v), \;\; |u|_K^2 := (u,u)_K, \;\; u,v \in V$$

Remark: In the case of vector-valued **K**, additional requirements on the position and amount of Dirichlet nodes might be necessary to make $(u,v)_K$ coercive on **V**. In linear elasticity applications, constants and infinitesimal rigid body motions can not be in the solution space **V**.

3.5 Network partition

In the proposed multiscale framework the network is divided into partitions. This partitioning is used to divide the computations into smaller domains, hence allowing less resource-intensive hardware to analyze. In the case of the paper models considered in Chapter 2 it makes sense to divide the domain into square partitions.

The grid partition considered is defined by uniform hypercubes with side length $H = 1/2, 1/4, \ldots$ of Ω:

$$\mathcal{T}_H = \{B_{H/2}(x) : x = (x_1, \ldots, x_d) \in \Omega \text{ and } H^{-1}x_i + 1/2 \in \mathbb{Z}^+, \;\; i = 1, \ldots, d\},$$

where the use of B_R guarantees that $\mathcal{T}_H$ is a true partition of Ω.

In the theoretical framework, the concept of a neighborhood of an element of the partition is necessary. These neighborhoods are defined using a set function $U : \Omega \to \Omega$:

$$\begin{aligned} U(\omega) := \{x \in \Omega : \exists T \in \mathcal{T}_H : x \in T, \overline{T} \cap \overline{\omega} \neq \varnothing\}, \\ U_k(\omega) = U(U_{k-1}(\omega)),\; U_0(\omega) = \omega. \end{aligned} \tag{3.7}$$

An illustration of T, $U(T)$, and $U_2(T)$ is provided in Figure 3.5.

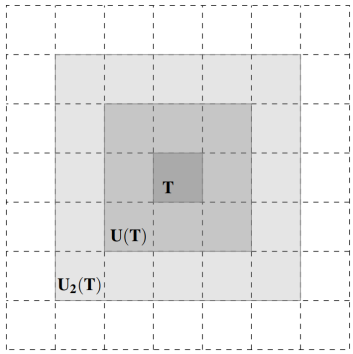

Figure 3.5: An illustration showing the growth of recursive use of the U operator.

Lower dimensional function space

On the partition $\mathcal{T}_H$ we can define the standard first-order continuous function space $\hat{Q}_H : \hat{V} \to \hat{V}$ as the union of all element spaces, $\hat{Q}_H(T),\ T \in \mathcal{T}$, that can be written as the product of continuous componentwise first-order polynomials (P_1) i.e,

$$\hat{Q}_H(T) = \{p : p(z_1, \ldots, z_d) = p_1(z_1)p_2(z_2)\cdots p_d(z_2), p_i \in P_1 \text{ for all } i\}.$$

In the case of two dimensions, this becomes the space of bilinear functions on $\mathcal{T}_H$. For brevity, we will assume that H is fixed when discussing this grid and will omit the H notation for components of these spaces. This space $\hat{Q}_H$ is a discrete space with a lower dimension, m, and can be defined as the span of the nodal basis functions $\hat{Q}_H = \text{span}(\{\phi_i\}_{i=1}^m)$.

Discrete versions of all these components are also used with the restrictions of $\hat{Q}_H$, and $\hat{Q}_H(T)$ to the nodal set $\mathcal{N}$ written as $\hat{V}_H$, and $\hat{V}_H(T)$ respectively. The nodal basis functions $\phi_1, \phi_2, \ldots, \phi_m$ are discretized as well, where φ_i is the restriction of ϕ_i to the nodal set for every i. Figure 3.6 presents a two-dimensional bilinear basis function (ϕ_i) interpolated by nodes in a network (φ_i).

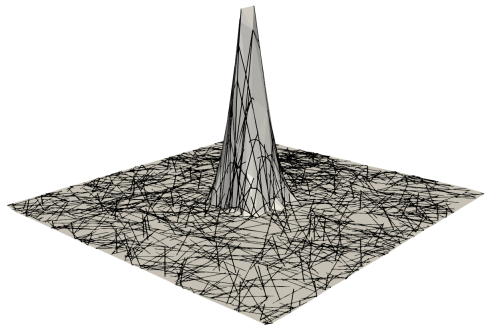

Figure 3.6: A two-dimensional network (black) interpolated (φ_i) onto the values of a bilinear basis function (ϕ_i). The gray shading was added for illustrative purposes.

Accurate interpolants

In both the iterative and multi-scale methods, interpolants are used. The multi-scale method presented in Chapter 4 is based on an accurate idempotent interpolant to define a fine-scale space. The interpolant constructed is based on the interpolant presented by Scott-Zhang [52]. In the iterative method presented in Chapter 5, an interpolant based on Clément in [53] is used to prove the stability of the convergence.

These interpolants map the solution space, V, to the lower dimensional function space $\hat{V}_H$. In particular it maps function from V into V. Under the assumption that the Dirichlet boundary conforms to the partition, we can write this space as:

$$V_H = \text{span}(\{\varphi_1, \ldots, \varphi_{m_0}\}), \tag{3.8}$$

where $\varphi_1, \ldots, \varphi_{m_0}$ are the interior nodal basis functions and $\varphi_{m_0+1}, \ldots \varphi_m$ are the nodal basis functions on the Dirichlet boundary. The two interpolants considered are both written in the following form:

$$I(v) = \sum_{k=1}^{m_0} (M_{T_k} \psi_k, v) \varphi_k,$$

with two different choices of dual functions $\psi_k \in \hat{V}_H$. Here, only the Scott-Zhang interpolant is presented.

Definition 10 (Scott-Zhang inspired interpolant)**:**

$$\begin{aligned} I_S(v) &= \sum_{k=1}^{m_0} (M_{T_k} \psi_k^S, v) \varphi_k, \\ \psi_k^S \in \hat{V}_H &: \ (M_{T_k} \psi_k^S, \varphi_j) = \delta_{k,j}, \ j = 1, \ldots, m. \end{aligned} \tag{3.9}$$

An important property of this interpolant is that it is idempotent: Let $v = V_H$, then:

$$I_S(v) = I_S \left(\sum_{i=0}^{m_0} \alpha_i \varphi_i \right) = \sum_{k=1}^{m_0} \left(M_{T_k} \psi_k^S, \sum_{i=0}^{m_0} \alpha_i \varphi_i \right) \varphi_k$$

$$= \sum_{k=1}^{m_0} \sum_{i=0}^{m_0} \alpha_i \left(M_{T_k} \psi_k^S, \varphi_i \right) \varphi_k = \sum_{k=1}^{m_0} \sum_{i=0}^{m_0} \alpha_i \delta_{k,i} \varphi_k = \sum_{k=0}^{m_0} \alpha_k \varphi_k = v.$$

Moreover, in **Paper D** Lemma 3.5, it is proven that this interpolant attains the following element local error bound:

Lemma 2: *If Assumption 2, 3, 4, 6 holds and $H \geq 4dR_0$, then for $v \in V$,*

$$H^{-1} |v - I_S(v)|_{M,T} + |I_S(v)|_{L,T} \leq C_d \sigma^{1/2} \mu |v|_{L,U_3(T)}, \ \forall T \in \mathcal{T}_H. \tag{3.10}$$

Note that U is the operator defined in (3.7) that defines neighborhoods with respect to the network partition.

CHAPTER 4

Localized Orthogonal Decomposition

The network models considered have similarities to steady-state heterogeneous diffusion (heat, elasticity) problems on the form:

$$-\text{div}(A\nabla u) = f,$$

where A is a positive-definite, rapidly varying coefficient matrix and f is some source term.

These variational problems lead to issues for standard numerical techniques, such as the finite element method, where variations must be resolved on the discretized scale. In the case of network problems, this requirement would result in systems the same size as the original problem. Multiscale methods aim to resolve this problem by constructing representative coarse scales of the heterogeneities and constructing approximations based on them.

The Localized Orthogonal Decomposition method (LOD) is a multiscale method [42], [54] based on the variational multiscale method [55]. These methods construct accurate coarse-scale spaces based on finite element inter-

polants. These spaces can be used in a Galerkin formulation, similar to the finite elements method, but unlike finite elements, do not require the heterogeneities to be resolved.

Theoretical [56]–[59] and numerical [60] development of the LOD method is ongoing. In particular, [47] presented a discrete version of the method and validated it for discrete network models posed on grid-type networks. **Paper A** continued this work and validated the method for fiber-based networks with a similar structure as the paper models.

The discrete LOD method proposed in [47] utilizes a synthetic coarse grid that spans the domain Ω the network resides in. The grid considered in this setting is the partition $\mathcal{T}_H$, with elements $T \in \mathcal{T}_H$ and associated shape functions $\{\varphi_i\}_{i=1}^m$ presented in detail in **Paper C**.

A naive finite element-type approach would be to use the discretized standard finite element basis (3.8), as follows:

$$\text{Find } u_H^{\text{FEM}} \in V_H \ : \ (Ku_H^{\text{FEM}}, v) = (f, v), \ \forall v \in V_H. \tag{4.1}$$

As we will later see, this approach leads to large errors. The main issue with this approach is that the basis of V_H can not resolve the model's heterogeneities [54].

The LOD method handles the heterogeneities of the model by resolving them by modifying the basis functions using orthogonal projections. Figure 4.1 presents a triangularization of a typical bilinear finite element shape function and an LOD basis function.

4.1 The ideal LOD method

The LOD method is a multi-scale method, which means the model problem is split into different scales. Here, the two scales considered are a representative coarse function space and a fine scale complement. In the proposed LOD method in **Paper D**, the fine scale space is defined as the kernel of the discrete Scott-Zhang interpolant (3.9).

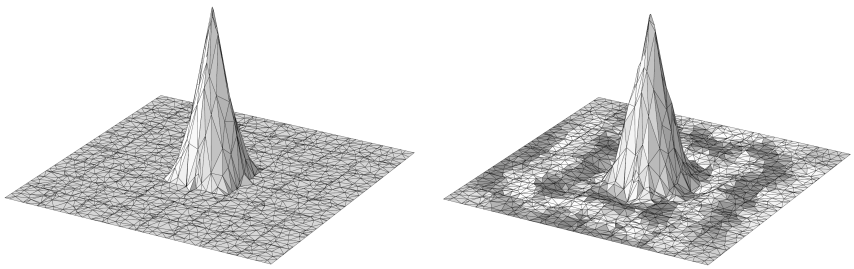

Figure 4.1: The left image shows a bilinear shape function, and the right shows a modified bilinear shape function used in an LOD method.

$$W = \ker(I_H^S) = \{v \in V : I_H^S(v) = 0\}. \tag{4.2}$$

The coarse function space, V_H^{ms}, is defined as the orthogonal complement to W with respect to the inner K-inner product:

$$V_H^{\text{ms}} = \{v \in V : (Kv, w) = 0,\ \forall w \in W\}.$$

This coarse space, V_H^{ms}, has the same dimension as V_H, and the ideal multiscale approximation, u_H^{ms} is formulated as:

$$\text{Find } u_H^{\text{ms}} \in V_H^{ms} :\ (Ku_H^{\text{ms}}, v) = (Mf, v),\ \forall v \in V_H^{\text{ms}}. \tag{4.3}$$

Unlike u_H^{FEM} in (4.1), u_H^{ms} is close to the correct solution in the following sense, with the following a priori error estimate proven in **Paper D**.

Lemma 3: *The error in the approximate solution* $\mathbf{u}_H^{ms}$*, defined in equation (4.3), fulfills*

$$|u - u_H^{ms}|_K \leq C_{\alpha,d,\mu,\sigma} H |f|_{M^{-1}},$$

where $|f|_{M^{-1}}^2 = (M^{-1}f, f)$*,* $C_{\mu,\sigma,\alpha}$ *denotes a dependence on the constants* μ, σ*, and* α *from Assumptions 3,4, and 5.*

The proof of this inequality follows from $u - u_H^{\text{ms}} \in W$, Galerkin orthogo-

nality, and the interpolation bound in Lemma 2:

$$|u-u_H^{\mathrm{ms}}|_K^2 = [\text{Galerkin orthogonality}] = (Ku, u-u_H^{\mathrm{ms}}) = (f, u-u_H^{\mathrm{ms}})$$

$$\Leftrightarrow |u-u_H^{\mathrm{ms}}|_K^2 \leq (M^{-1}f, M(u-u_H^{\mathrm{ms}})) \leq |f|_{M^{-1}}|u-u_H^{\mathrm{ms}}|_M. \tag{4.4}$$

If we plug $v = u - u_H^{\mathrm{ms}}$ into Lemma 2 we get:

$$H^{-1}|u-u_H^{\mathrm{ms}} - I_H^S(u-u_H^{\mathrm{ms}})|_{M,T} + |I_H^S(u-u_H^{\mathrm{ms}})|_{L,T} \leq C_d\sigma^{1/2}\mu|u-u_H^{\mathrm{ms}}|_{L,U_3(T)}$$

$$\Leftrightarrow H^{-1}|u-u_H^{\mathrm{ms}} - 0|_{M,T} + |0|_{L,T} \leq C_d\sigma^{1/2}\mu|u-u_H^{\mathrm{ms}}|_{L,U_3(T)}$$

$$\Leftrightarrow H^{-1}|u-u_H^{\mathrm{ms}}|_{M,T} \leq C_d\sigma^{1/2}\mu|u-u_H^{\mathrm{ms}}|_{L,U_3(T)}$$

$$\Leftrightarrow |u-u_H^{\mathrm{ms}}|_{M,T} \leq C_d\sigma^{1/2}\mu H|u-u_H^{\mathrm{ms}}|_{L,U_3(T)}$$

$$\Rightarrow |u-u_H^{\mathrm{ms}}|_M \leq C_d'\sigma^{1/2}\mu H|u-u_H^{\mathrm{ms}}|_L \leq C_d'\sigma^{1/2}\alpha^{-1/2}\mu H|u-u_H^{\mathrm{ms}}|_K \tag{4.5}$$

The last step is taking the sum of the squares over all $T \in \mathcal{T}_H$ and multiplying by the dimension-specific number of overlaps occurring when summing over $U_3(T)$ instead of T. Plugging (4.5) in (4.4) and dividing by $|u-u_H^{\mathrm{ms}}|_K$ finishes the proof.

From Lemma 3, it is clear that u_H^{ms} is accurate and converges when $H \to 0$. This approximation can be computed by finding a basis for the multi-scale space V_H^{ms}, and is defined using the fine-scale projection operator $Q : V \to W$:

$$(KQv, w) = (Kv, w),\ \forall w \in W,\ \forall v \in V. \tag{4.6}$$

The coarse scale V_H^{ms} can then be written as:

$$V_H^{\mathrm{ms}} = \{v - Qv :\ v \in V_H\},$$

with any vector $v \in V$ having the unique decomposition

$$v = (v - Qv) + Qv \in V_H^{ms} \oplus W.$$

Using this projection operator, we can construct the following basis of

$V_H^{ms} = \text{span}(\{\varphi_i - Q\varphi_i\}_{i=1}^m)$ from the discretized finite element shape functions $\{\varphi_i\}_{i=1}^m$.

Computationally, this basis does not make sense as calculating the correction term $-Q\varphi_i$ requires a system on the size of the original problem to be solved. However, as shown in **Paper D**, the correction term $-Q\varphi_i$ decays exponentially, allowing them to be computed locally.

4.2 Localization of the LOD basis

In the proposed localization in **Paper D**, the operator K is assumed to have a node-wise decomposition as follows:

Assumption 7 (Node-wise composition)**:** *The matrix K can be written as a sum, $K = \sum_{x\in\mathcal{N}} K_x$, of operators $K_x : \hat{V} \to \hat{V}$, where K_x are symmetric positive semi-definite and have support on x and nodes adjacent to x.*

From this assumption, it is possible to formulate a local version of the K-norm $|u|_{K,\omega}^2 = \sum_{x_i\in N(\omega)}(K_i u, u)$, which will be used later. Moreover, with this assumption, we can decompose the projection operator element-wise as $Q = \sum_{T\in\mathcal{T}} Q_T$, where $Q_T : V \to W$ satisfies:

$$(KQ_T v, w) = (K_T v, w),\ \forall w \in W,\ \forall v \in V,$$

where $K_T = \sum_{x\in N(T)} K_x$, because $K = \sum_{T\in\mathcal{T}} K_T$.

The localized projection operator evaluated in **Paper D** is defined by restricting Q_T to components in $U_k(T)$, where k is a localization parameter, by solving:

$$\begin{aligned} (KQ_T^k v, w) &= (K_T v, w),\ \forall w \in W(U_k(T)), \\ W(\omega) &= \{w \in W :\ w(x_i) = 0, \forall x_i \in N(\Omega \setminus \omega)\}. \end{aligned} \tag{4.7}$$

These projection operators have small support, and evaluating $Q_T^k v$ for a v translates to solving a linear system on the support $U_k(T)$. Moreover, this restricted version of Q_T is accurate, with the following bound proven in **Paper**

D with respect to k:

Lemma 4: *Under the network assumptions, model assumptions, and* $H \geq 8dR_0$*, we have that for any* $v \in V$ *it holds:*

$$|(Q_T - Q_T^k)v|_K \leq C_{\mu,\sigma,\alpha,\beta} \exp(-kC)|v|_{K,T},$$

for constants $C_{\mu,\sigma,\alpha,\beta}$ *and* C*.*

The global projection operator, Q_H, can then be approximated by $Q_H^k = \sum_{T\in\mathcal{T}} Q_T^k$, and the approximate basis for the coarse scale is defined as:

$$V_H^{\mathrm{ms},k} = \{(1 - Q_H^k)v : \ v \in V_H\}.$$

The LOD approximation, $u_H^{\mathrm{ms},k}$, is attained by solving:

$$\text{Find } u_H^{\mathrm{ms},k} \in V_H^{ms,k} : \ (Ku_H^{\mathrm{ms},k}, v) = (Mf, v), \ \forall v \in V_H^{\mathrm{ms},k}. \tag{4.8}$$

With the main result of paper **Paper D** being the proof of the following a priori error estimate.

Theorem 1: *Under the network assumptions, model assumptions, and* $H \geq 8dR_0$*, the error in the approximate solution* $u_H^{ms,k}$*, defined in equation* (4.8)*, fulfills*

$$|u - u_H^{ms,k}|_K \leq C^1_{\mu,\sigma,\alpha,\beta} \left(H + \exp(-kC^2_{\mu,\sigma,\alpha,\beta})\right) |f|_{M^{-1}},$$

for some constants $C^1_{\mu,\sigma,\alpha,\beta}$ *and* $C^2_{\mu,\sigma,\alpha,\beta}$*.*

4.3 Numerical evaluation

Three numerical examples are presented. The first two examples are presented in **Paper D**, and are based on the network with uniform distribution presented in Chapter 3, Figure 3.2. For the third example, presented originally in [44], the LOD method is used to solve the tensile stiffness simulation in **Paper B**.

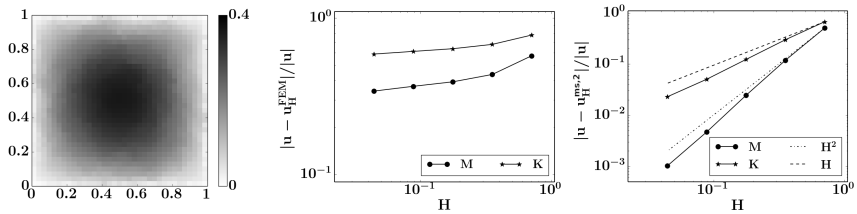

Figure 4.2: The solution of the diffusion problem, along with the convergence results for the finite element style and LOD approximation.

Diffusion problem

A two-dimensional diffusion problem on $\Omega = [0,1]^2$ is considered where the following weighted version of the L-operator is considered:

$$(Kv, w) = \sum_{x_i \in \mathcal{N}(\Omega)} (K_i v, w),$$
$$(K_i v, w) = \frac{1}{2} \sum_{i \sim j} \gamma_{ij} \frac{(v(x_i) - v(x_j))(w(x_i) - w(x_j))}{|x_i - x_j|},$$

where the weights $\gamma_{ij} \in [0.1, 1]$ are chosen from a uniform distribution. For this problem, the entire boundary has zero Dirichlet boundary conditions with constant right-hand side data $f = \mathbf{1}$.

As the reference solution, the problem was solved using a linear solver (see Figure 4.2). This solution is compared to the approximations made with the naive approach in (4.1) to the corresponding LOD approximations (4.8) with localization parameter $k = 2$. Figure 4.2 presents the convergence results for the different H. From these results, it is clear to observe a typical convergence plateau for the naive approach. In contrast, the LOD method obtains the theoretical convergence in Theorem 1 with respect to the K-norm. Moreover, H^2 convergence is observable in the M-norm, which is consistent with an optimal first-order finite element method.

Table 4.1: Structural parameters of the wire mesh structural problem

Explanation	Parameter	Value
Radius of wire	r_w	2.5 mm
Cross-section Area	A	πr_w^2
Young's modulus	E_A, E_B	210GPa
Second moment of area	I	$0.25\pi r_w^4$

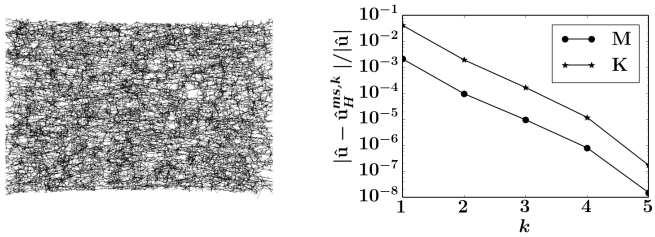

Figure 4.3: The solution of the two-dimensional equilibrium tensile simulation, and the k-convergence results for the LOD approximation.

Structural problem

In **Paper D** two structural problems are analyzed, and one is presented here. In this example, the two-dimensional network is modeled as a mesh of wires with the Euler-Bernoulli model presented in Chapter 2. Table 4.1 presents the structural parameters used. In the specific problem, the network is strained on two opposite sides 50 %, and the equilibrium is found. Because the right-hand side is zero (no applied force), the ideal LOD approximation is exact. This means that the only error introduced is based on localization, and we should see exponential convergence with respect to k. An illustration of the exact solution to this problem, along with the k convergence results, are presented in Figure 4.3.

The results from this analysis show that we do have exponential convergence with respect to k, consistent with Theorem 1. It also shows that exceedingly good approximations can be attained for a localization factor of $k = 2$,

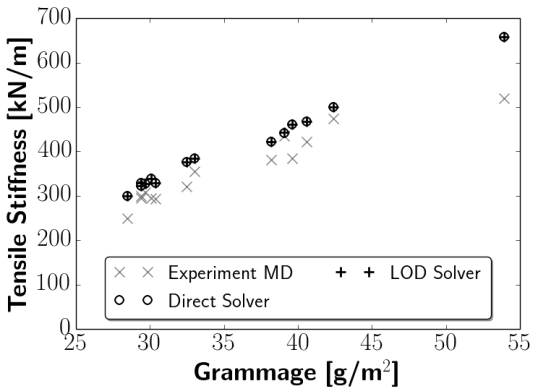

Figure 4.4: Tensile stiffness simulations using the LOD method.

illustrating that the LOD method can work with a high degree of localization.

Validated paper model

The tensile stiffness simulation in the machine direction in **Paper B** was solved with the LOD method in [44]. Unlike the previous example, the validated paper models are three-dimensional. These models have practically no thickness compared to the width and length of the sheet, and this geometric irregularity is resolved by only having one element through the thickness of the sheet. For this example, $16 \times 16 \times 1$ coarse elements are used, with localization parameter $k = 2$. In this numerical example, each sheet is evaluated once, and nodes are placed on the boundary to reduce boundary effects. Figure 4.4 shows the results after these slight modifications, and the results show that the method produces almost identical results as the exact solution. In each simulation, less than one percent difference in the predicted tensile stiffness was observed for the LOD approach compared to the exact solution.

4.4 The LOD method for the wave equation

In **Paper E**, the theory presented for elliptic-type problems was extended to a hyperbolic-type problem. The problem considered is the following wave propagation problem posed on a spatial network. Find $u : [0,T] \to V$ such that

$$\begin{aligned} MD_t^2 u(t) + Ku(t) &= Mf(t), \text{ in } \Omega \\ u(t) &= 0, \text{ on } \Gamma \\ u(0) = g,\, D_t u(0) &= h, \text{ in } \Omega \end{aligned} \tag{4.9}$$

where M is the network operator, K is an elliptic-type stiffness matrix, and $g, h \in \hat{V}$, $f : \mathbb{R}_0^+ \to \hat{V}$ are the data of the problem.

This problem has the corresponding weak form:

$$(MD_t^2 u(t), v) + (Ku(t), v) = (Mf(t), v),\ 0 < t \leq T,\ \forall v \in V. \tag{4.10}$$

and from this it is possible to show the following important energy conservation law.

Theorem 2: *Let $u : [0,T] \to V$ be a sufficiently smooth solution to* (4.10)*, with $f = 0$, then:*

$$\mathcal{E}(t) := \frac{1}{2}\left(|D_t u(t)|_M^2 + |u(t)|_K^2\right) = \mathcal{E}(0),$$

is constant.

Proof. The proof follows from plugging in $v = D_t u(t)$ into (4.10):

$$(MD_t^2 u(t), D_t u(t)) + (Ku(t), D_t u(t)) = (Mf(t), v) = 0. \tag{4.11}$$

To prove the statement, we will use that for any self-adjoint operator $A : V \times V \to \mathbb{R}$ on a finite-dimensional Hilbert space the following identity holds:

$$(Av, D_t v) = \tfrac{1}{2} D_t (Av, v)$$

This can be seen by using the spectral decomposition ($\{w_i, \lambda_i\}_{i=1}^n$) of the operator A:

$$(Au(t), D_t u(t)) = \left(\sum_{i=1}^n \lambda_i (u(t), w_i) w_i, D_t u(t) \right) = \sum_{i=1}^n \lambda_i (u(t), w_i)(w_i, D_t u(t))$$

$$= \left[(u(t), w_i)(w_i, D_t u(t)) = \tfrac{1}{2} D_t (u(t), w_i)^2 \right] = \frac{1}{2} D_t \sum_{i=1}^n \lambda_i (u(t), w_i)(u(t), w_i)$$

$$= \frac{1}{2} D_t \left(\sum_{i=1}^n \lambda_i (u(t), w_i) w_i, u(t) \right) = \frac{1}{2} D_t (Au, u).$$

This identity holds for both M (diagonal) and K (Assumption 5), and more specifically we have:

$$(MD_t^2 u(t), D_t u(t)) = \frac{1}{2} D_t |D_t u|_M^2 \quad (Ku(t), D_t u(t)) = \frac{1}{2} D_t |u|_K^2$$

which used in (4.11), implies

$$D_t \frac{1}{2} (|D_t u|_M^2 + |u|_K^2) = D_t \mathcal{E}(t) = 0 \Rightarrow \mathcal{E}(t) = \mathcal{E}(0)$$

□

Temporal discretization

This problem can be discretized temporarily using a uniform stepsize:

$$0 = t_0 < t_1 < \ldots < t_N = T, \quad t_i - t_{i-1} = \tau,$$

where $u^i = u(t_i)$ and $f^i = f(t_i)$. The corresponding discrete temporal problem considered takes the following form: find $\{u^i\}_{i=0}^N \in V$:

$$(M \partial_t \bar{\partial}_t u^i, v) + (K \tfrac{1}{2} (u^{i+1/2} + u^{i-1/2}), v) = (Mf^i, v), \ \forall v \in V, \tag{4.12}$$

where $\partial_t u^i = (u^{i+1} - u^i)/\tau$, $\bar{\partial}_t u^i = (u^i - u^{i-1})/\tau$, and $u^{i+1/2} = \frac{1}{2}(u^i + u^{i+1})$. Under regularity assumptions on the data, we have:

$$|\partial_t u^i - D_t(u(t_i + 1/2))|_M + |u^{i+1/2} - u(t_i + 1/2)|_K \leq C\tau^2.$$

by following the same steps (specifically Taylor arguments) as the proof for Theorem 5.8 in **Paper E** with $\rho^n = 0$, $\theta^n = u(t_i) - u^i$. Moreover, the scheme conforms to the following energy conservation law (by following similar steps as in [61, Lemma 13.2]):

$$|\partial_t u^i|_M^2 + |u^{i+1/2}|_K^2 = |\partial_t u^0|_M^2 + |\partial_t u^{1/2}|_K^2$$

Solutions to problems discretized with this scheme can be solved numerically (V is a discrete space) by solving N elliptic-type linear systems on the form (3.4) with different right-hand sides.

The LOD method presented earlier in this chapter was shown to produce accurate approximations of such problems. Moreover, the modified shape functions can be reused to solve systems efficiently with different right-hand sides. In practice, this results in a computationally heavy offline stage where the modified shape functions are solved and an efficient online stage where the LOD approximations are used to approximate the solution to multiple linear systems.

The LOD approximation proposed, $\{u_{H,k}^{\mathrm{ms},i}\}_{i=0}^N \in V_{H,k}^{\mathrm{ms}}$, is defined as:

$$(M\partial_t \bar{\partial}_t u^{\mathrm{ms},i} + (K\tfrac{1}{2}(u_{H,k}^{\mathrm{ms},i+1/2} + u_{H,k}^{\mathrm{ms},i-1/2}), v) = (Mf^i, v),\ \forall v \in V_{H,k}^{\mathrm{ms}}. \quad (4.13)$$

This approximation was analyzed in **Paper E**, under the network and model assumptions in **Paper C**. In **Paper E**, it was shown that the approximation followed a similar conservation law to (4.12):

$$|\partial_t u_{H,k}^{\mathrm{ms},i}|_M^2 + |u_{H,k}^{\mathrm{ms},i+1/2}|_K^2 = |\partial_t u_{H,k}^{\mathrm{ms},0}|_M^2 + |\partial_t u_{H,k}^{\mathrm{ms},1/2}|_K^2,\ \ i = 0, 1, \ldots, N$$

and that the approximation was accurate and obtained the following a priori

error bound

$$\max_i \left(|\partial_t u_{H,k}^{\mathrm{ms},i} - D_t(u(t_i+1/2))|_M + |u_{H,k}^{\mathrm{ms},i+1/2} - u(t_i+1/2)|_K \right) \leq C(H+\tau^2). \tag{4.14}$$

Numerical evaluation

The LOD method (4.13) and the error bound 4.14 presented in **Paper E** were evaluated numerically. Two of the three numerical experiments presented in **Paper E** are presented here. The same network is used in these experiments and is generated using the same methodology as the networks in Chapter 3, Figure 3.2. The network has the two-dimensional domain $\Omega = [0,1]^2$, uniform placement and orientation of the line segments of length $r = 0.07$, and a density of $|1|_M^2 = 700$).

In the two numerical examples, the LOD method used to approximate the problems has localization parameter $k = \log_2(1/H)$ and is evaluated for grid sizes $H = 2^{-i}$, $i = 2,3,4,5$. Moreover, a slightly modified interpolant was used in the experiments. The dual in the Scott-Zhang interpolant (3.9) is the average of the elements where the nodal basis function has support instead of taking one arbitrary element. This was done to make the interpolant symmetric, which led to substantial improvement for larger element sizes in particular. It should be mentioned that taking the average of the four duals as a dual for the interpolant in the LOD method will still obtain the convergence bound (4.14) by linearity.

The homogeneous wave equation

The first model problem is constructed to have a known exact solution. This is done by considering a homogeneous problem with data based on the generalized eigenvalue problem: $Kw = \lambda w$. In this case, the sixth eigenpair $\{\lambda_6 \approx 16, w_6\}$ is chosen, and the following problem is considered:

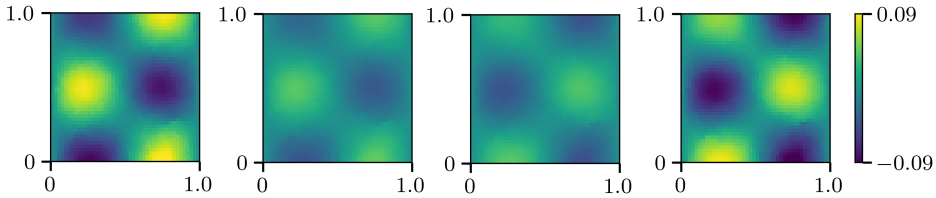

Figure 4.5: The exact solution to (4.15) at $t = \alpha\pi/\sqrt{\lambda_6}$, $\alpha = 0, \frac{1}{3}, \frac{2}{3}, 1$.

$$\begin{cases} MD_t^2 u + Ku = 0,\ t \in [0, \pi/\sqrt{\lambda_6}] \\ u = 0,\ x \in \Gamma = \{x \in \mathcal{N} : x_1 \in \{0,1\}\}, \\ u(0) = w_6,\ D_t u(0) = 0. \end{cases} \tag{4.15}$$

The exact solution to this problem is $u(t) = \cos(\sqrt{\lambda_6}t)w_6$ and the temporal interval considered is half the period of this exact solution. An illustration of this solution at different times is presented in Figure 4.5.

The exact solution is compared to the LOD approximation (4.13) with $\tau = 10^{-3}$, and initial conditions chosen using Remark 5.11 in **Paper E**:

$$u_{H,k}^{\mathrm{ms},0} = u(0) = w_6,\ \ u_{H,k}^{\mathrm{ms},1} = \left(w_6 - \lambda_6 \frac{\tau^2}{2} w_6\right),$$

where $M^{-1}Ku(0) = M^{-1}Kw_6 = \lambda_6 M^{-1}Mw_6 = \lambda_6 w_6$. The H-convergence analysis for these evaluations is presented in Figure 4.6, where the theoretical order of convergence is observed in both M-norm and K-norm (4.14).

The inhomogeneous elastic wave equation

In the second numerical example, the network is interpreted as a mesh of steel wires fixed at one side with a varying applied vertical force. This steel mesh is modeled using the Euler-Bernoulli model in Chapter 2, with wires of radii 0.5 mm and Young's modulus 210 GPa. The specific problem considered takes the following form:

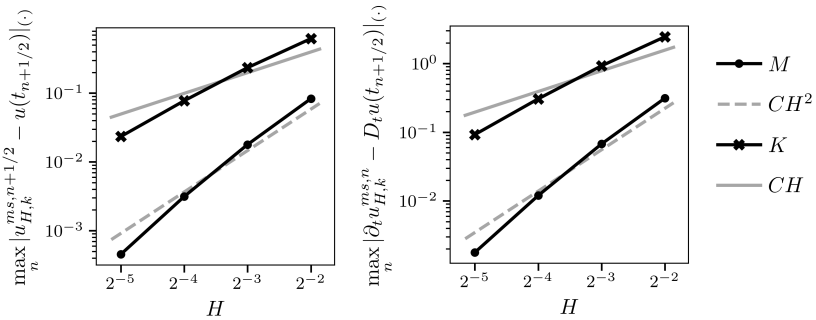

Figure 4.6: The convergence of the LOD method. In the left figure, the error bound in (4.14) is observed with H convergence in the K-norm, and in the right figure, the error bound in is surpassed with H^2 convergence in the M-norm.

$$\begin{cases} \mathbf{M}D_t^2\mathbf{u} + \mathbf{K}\mathbf{u} = \mathbf{M}\left(10^5 x_1^2 \sin(0.4\pi t)\mathbf{1}_z\right),\ t \in [0,10] \\ \mathbf{u} = 0,\ x \in \Gamma = \{x \in \mathcal{N} : x_1 = 0\}, \\ \mathbf{u}(0) = 0,\ D_t\mathbf{u}(0) = 0, \end{cases} \tag{4.16}$$

where $\mathbf{M}$ represents an application of the mass matrix in each coordinate direction, and $\mathbf{1}_z(x) = [0,0,1]^T$.

In this numerical example, the approximation is compared to the reference solution u^n, defined by (4.12) with $\tau = 0.01$. Figure 4.7 presents the reference solution at three points in time, and Figure 4.8 presents the convergence of the LOD approximation to the reference solution. From these results it is clear that the method obtains optimal order convergence in both $\mathbf{M}$-norm and $\mathbf{K}$-norm.

Figure 4.7: Reference solution $\mathbf{u}^n$ of (4.16) at $t = 0, 5, 10$. The surface is the network model overlayed on a transparent triangularization for visualization purposes. The square outline is the boundary of the non-displaced network.

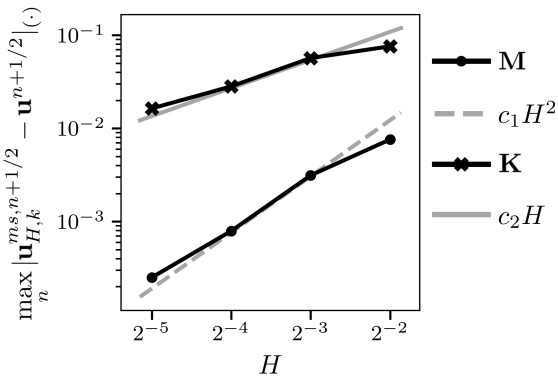

Figure 4.8: The convergence of the LOD method to the reference solution $\mathbf{u}^n$ of (4.16), where the LOD approximation converges linearly with respect to H in the $\mathbf{K}$-norm and quadratically in the $\mathbf{M}$-norm.

CHAPTER 5

Domain decomposition

In Chapter 2, **Paper B**, and **Paper F** network models with hundreds of thousands of beams are evaluated, and solving the associated linear systems is computationally demanding. The previous chapter formulated an approximation on some discretization scale H with a multi-scale approach. This chapter presents the alternative iterative method in **Paper C**. This iterative approach splits the model into problems on smaller domains and iteratively finds better approximations that converge to the exact solution. This restriction to smaller subdomains reduces the computational domain for each problem, thus requiring less memory to solve.

5.1 Preconditioned conjugate gradient

An iterative solver finds a sequence of approximations, $\{u_k\}_{k=0}$, such that $|u_k - u| \to 0$. The method proposed for network models is based on the standard conjugate gradient algorithm (CG) algorithm presented in Algorithm 1

from [62], with the K-scalar product, on the preconditioned problem:

$$\text{Find } u \in V: \ (BKu, v) = (Bf, v), \ \forall v \in V,$$

where B is a preconditioner later introduced, and BK [$= P$ in **Paper C**] is symmetric positive definite with respect to the K inner product on V. Algorithm 2 presents the same preconditioned conjugate gradient (PCG) algorithm but optimized to minimize matrix multiplications.

Algorithm 1 Preconditioned conjugate gradient algorithm

$r_0 \leftarrow B(f - Ku_0)$ [u_0 some initial guess]
$p_0 \leftarrow r_0$
for $j = 0, 1, \ldots$ until convergence **do**
  $\alpha_j \leftarrow (r_j, r_j)_K / (BKp_j, p_j)_K$
  $u_{j+1} \leftarrow u_j + \alpha_j p_j$
  $r_{j+1} \leftarrow r_j - \alpha_j BKp_j$
  $\beta_j \leftarrow (r_{j+1}, r_{j+1})_K / (r_j, r_j)_K$
  $p_{j+1} \leftarrow r_{j+1} + \beta_j p_j$
end for

The PCG algorithm is efficient if $BK \sim I$, with the following classical convergence result [62, p. 204] obtained based on the spectral bounds of BK; if $\lambda_{min} > 0$ and $\lambda_{max} > 0$:

$$\lambda_{min} \leq \frac{(BKu, u)_K}{(u, u)_K} \leq \lambda_{max},$$

then

$$|u - u_k|_K = 2 \left(\frac{\sqrt{\kappa} - 1}{\sqrt{\kappa} + 1} \right)^k |u - u_0|_K,$$

where $\kappa = \lambda_{max} / \lambda_{min}$, and u_0 is the initial guess used in the PCG algorithm.

Algorithm 2 Optimized preconditioned conjugate gradient algorithm

$r_0 \leftarrow B(f - Ku_0)$
$p_0 \leftarrow r_0$
$z_0, q_0 \leftarrow Kr_0$
$w_0 \leftarrow B(q_0)$
for $j = 0,\ 1,\ \ldots$ until convergence **do**
  $\alpha_j \leftarrow (z_j, r_j)/(w_j, q_j) \quad [z_j = Kr_j,\ w_j = BKp_j,\ q_j = Kp_j]$
  $u_{j+1} \leftarrow u_j + \alpha_j p_j$
  $r_{j+1} \leftarrow r_j - \alpha_j w_0$
  $z_{j+1} \leftarrow Kr_j$
  $\beta_j \leftarrow (z_{j+1}, r_{j+1})/(z_j, r_j)$
  $p_{j+1} \leftarrow r_{j+1} + \beta_j p_j$
  $q_{j+1} \leftarrow z_{j+1} + \beta_j q_j$
  $w_{j+1} \leftarrow Bq_{j+1}$
end for

5.2 Domain decomposition preconditioner

The preconditioner used in the proposed PCG method is constructed using the same partition presented in Chapter 3 with associated finite element space $\{\mathcal{T}_H, V_H\}$, and grid nodes $\{y_k\}_{k=1}^m$.The preconditioner is inspired by [38] for elliptic problems posed on continuums and is composed of two parts: a rough global approximation and multiple local approximations.

The coarse global approximation is the naive approach presented in the previous chapter in (4.1), where $B_0 : V \to V_H$ is defined implicitly as:

$$B_0(r) = \tilde{u}_0 \ \Leftrightarrow\ \text{Find } \tilde{u}_0 \in V_H \ :\ (K\tilde{u}_0, v_H) = (r, v_H),\ \forall v_H \in V_H. \tag{5.1}$$

The notation of r in the definition $B_0(r)$ is used to emphasize that this function is called with arguments similar in structure to the residual in the PCG algorithm. As mentioned, this operator finds approximations under weighted averages and is not good at resolving details. It does not matter in this setting as these details are resolved in the other local components of B.

The local components of B, B_i, are defined on smaller computational domains of the network. These domains are defined around each grid-point y_k, more specifically $U(y_k) = U(\{y_k\})$. This domain can be seen as all elements whose closure contains the grid node (y_k) or, alternatively, the support of the nodal basis function in the node. This notation is used to define the local computational spaces V_k as the spaces of functions that vanish outside of $U(y_k)$.

With these spaces defined, we can define the localized parts, $B_i : V \to V_i$, of the preconditioner as:

$$B_i(r) = \tilde{u}_i \Leftrightarrow \text{Find } \tilde{u}_i \in V_i \ : \ (K\tilde{u}_i, v_i) = (r, v_i), \ \ \forall v_i \in V_i, \ i = 1, \dots \ m,$$

and this can be re-written in strong form as:

$$[K]_{U(y_i)}\tilde{u}_i = [r]_{U(y_i)},$$

where $[K]_{U(y_i)}\tilde{u}_i = [K\tilde{u}_i]_{U(y_i)}$ denotes the restriction of the function in V to the function only defined on the nodes in the space $U(y_i)$. In these cases, the approximation $[K^{-1}r]_{U(y_i)} \approx [B_i(r)]_{U(y_i)}$ is accurate if the values of r close to $U(y_i)$ but not contained in $U(y_i)$ are small.

The complete preconditioner used in the proposed PCG algorithm in **Paper C** is:

$$Bv = \sum_{k=0}^{m} B_i v.$$

Moreover, in **Paper C** it is proven that:

$$\frac{\alpha}{C_d \beta \sigma \mu^2} \leq \frac{(BKu, u)_K}{(u, u)_K} \leq C_d,$$

where C_d is a constant depending on the dimension of the domain Ω. This gives the following theorem (Theorem 4.4, **Paper C**):

Theorem 3: *Under the network assumptions, model assumption 5, and* $H \geq$

$2R_0$ then the preconditioned conjugate gradient approximation $u^{(\ell)}$ fulfills

$$|u-u^{(\ell)}|_K \leq 2\left(\frac{\sqrt{\kappa}-1}{\sqrt{\kappa}+1}\right)^{\ell}|u-u^{(0)}|_K,$$

where $\sqrt{\kappa} = C_d\beta^{1/2}\alpha^{-1/2}\sigma^{1/2}\mu$.

5.3 Numerical examples

Two numerical examples are presented for the domain decomposition method. The first example is part of the numerical example performed in **Paper C**, where the sharpness of the constant C_d in Theorem 3 is evaluated. The second example is the domain decomposition method used to evaluate the bending stiffness of the paperboard model presented in Chapter 2 and **Paper F**.

Analysis of the constant C_d

We consider a heat conductivity problem for two types of two-dimensional networks: an equidistant grid and a fiber network on the domain $\Omega = [0,1]^2$. The PCG method is applied to these problems, and the convergence rate is analyzed.

The first grid network is composed of $(2^9+1)^2$ nodes and is used to estimate the dimensional constant C_d in Theorem 3 by evaluating μ, σ for the grid network as in Chapter 3, together with the convergence rate when $K = L$. The convergence rates are evaluated by finding $\tau, \bar{\tau}$ such that:

$$\begin{aligned} \tau_{(\ell)} &:= \frac{|u-u^{(\ell-1)}|_K}{|u-u^{(\ell)}|_K} \leq \tau,\ l = 2,\ \ldots, \max \text{ it} \\ \bar{\tau} &:= \frac{1}{\max \text{ it}} \sum_{i=2}^{\max \text{ it}} \tau_{(\ell)} \end{aligned} \tag{5.2}$$

These constants $\mu, \sigma, \bar{\tau}$, can then be used to estimate the constant C_d in Theo-

Table 5.1: Investigation of the constant C_d using the average convergence rates, $\bar{\tau}$, and the geometrical constants σ and μ for the regular grid network.

	$H^{-1}=4$	$H^{-1}=8$	$H^{-1}=16$	$H^{-1}=32$
σ	1.0	1.0	1.1	1.1
μ	0.45	0.47	0.48	0.51
C_d	3.2	3.5	3.5	3.2

rem 3 by:

$$\bar{\tau} := \frac{\sqrt{\kappa}-1}{\sqrt{\kappa}+1},\ \sqrt{\kappa} = C_d \mu \sqrt{\sigma} \ \Leftrightarrow\ C_d = \frac{1+\bar{\tau}}{\mu\sqrt{\sigma}(1-\bar{\tau})}, \tag{5.3}$$

The problem considered is $Lu = M1$, with the entire boundary having zero Dirichlet conditions. The convergence rate of the PCG method for this problem is presented in Table 5.2, and the result of the C_d study is presented in Table 5.1. From this analysis, we get that $C_d \approx 3.5$.

This constant, $C_d \approx 3.5$, is then used to predict the convergence rate for a fiber network comparable to the uniformly distributed fiber network presented in Chapter 3 with $K = L$ on the same problem $Ku = M1$. From the estimate of C_d, the convergence rate of the domain decomposition method can be compared to:

$$\tilde{\tau} := \frac{\sqrt{\kappa}-1}{\sqrt{\kappa}+1},\ \sqrt{\kappa} = 3.5\sqrt{\sigma}\mu.$$

The numerical evaluation of the convergence rate is presented in Table 5.2, and the comparison is presented in Table 5.3 using the constants μ, σ from Chapter 3. This comparison shows that the geometric constant is sharp for all but the finest coarse grid $\mathcal{T}_H$, where the PCG method converges faster than the estimate.

Table 5.2: The PCG method's average and worst convergence rates, $(\bar{\tau}, \tau)$, for different heat conductivity problem ($K = L$).

Problem	$H^{-1} = 4$	$H^{-1} = 8$	$H^{-1} = 16$	$H^{-1} = 32$
Grid	(0.18,0.31)	(0.25,0.33)	(0.27,0.32)	(0.28,0.31)
Fiber	(0.29,0.48)	(0.33,0.43)	(0.39,0.49)	(0.42,0.47)

Table 5.3: Comparing convergence rate estimates, $\tilde{\tau}$, with average convergence rates, $\bar{\tau}$, in numerical experiments for a fiber based network.

	$H^{-1} = 4$	$H^{-1} = 8$	$H^{-1} = 16$	$H^{-1} = 32$
$\bar{\tau}$	0.29	0.33	0.39	0.42
$\tilde{\tau}$	0.27	0.35	0.45	0.60

Full paperboard simulation

As mentioned in Chapter 2, the bending stiffness of the full 400 g/m^2 paperboards is simulated. This results in network models roughly four times the problems considered in that chapter. A direct approach is impossible on consumer hardware with 128 GB of memory (RAM). With the results from Chapter 2 in mind, the four-point method is considered on paperboards with dimensions 32 mm $\times$ 4 mm.

For the PCG method, a FE grid ($\mathcal{T}_H$) has to be defined. Here, the grid containing the domain of the model with an element size of 1 mm $\times$ 1 mm is chosen, with one element through the thickness of the model. This choice was determined experimentally, where smaller element sizes reduced performance. The resulting computational domain in the PCG method is 2 mm $\times$ 2 mm, requiring roughly 12 Gb of memory to solve for the paperboard composed entirely of kraft. The preconditioner requires this computation for each $\{B_i\}_{i=1}^m$. These can be performed in parallel, and the method is well-suited for computer clusters.

An initial guess, u_0, has to be chosen in the PCG algorithm. This was done by interpolating the solution of a Timoshenko beam representing the entire deformed sheet. Figure 5.1 shows the interpolation of a 200 g/m^2 network

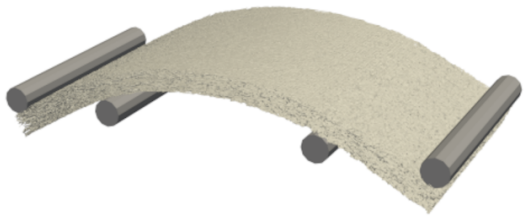

Figure 5.1: Interpolated fiber-based approximations for the four-point example in Figure 2.8.

Table 5.4: Replicated experimental results in [45] with fiber-based simulations using a four-point methodology on 400 g/m^2 paper models dimensions 32 mm $\times$ 4 mm enabled with the proposed domain decomposition method.

Weight Fraction	Simulated S_b	Experimental S_b
0 %	114 mNm	113 mNm
25%	169 mNm	170 mNm
50%	162 mNm	164 mNm
75%	120 mNm	128 mNm
100%	71.8 mNm	74 mNm

model for a four-point simulation, and **Paper F** presents this interpolation in detail.

With this initial guess, u_0, the PCG method was used to find subsequently better approximations until convergence. The simulated bending stiffness compared to the four bending stiffness experiments performed in [45] is presented in Table 5.4. From these results, it is clear that it is possible to simulate the bending stiffness on these scales with the PCG algorithm using consumer hardware and that the micro-mechanical simulations provide representative results.

CHAPTER 6

Summary and Future Work

This chapter will summarize the content of this thesis and discuss potential future development.

Summary

In Chapter 2 a network-based paper model was used to evaluate three-ply paperboards consisting of CTMP and kraft pulp. The shape of each paper fiber in the model was based on detailed pulp analysis. The structural parameters of this model were deduced using tensile experiments from [45] and Perkins' formula for tensile stiffness [46]. Both tensile stiffness and bending stiffness were evaluated for eleven 200 g/m^2 three-ply paperboards with various weight ratios in the three layers. These results clearly show that the linear network model predicts the macro-scale theoretical scaling for the models considered.

The model was based on experimental data accessible—and provided by—paper product companies without the need for specialized experiments or ex-

tensive parameter fitting. These results include the simulation of the bending stiffness of paperboard using micro-scale models, where literature on out-of-plane simulations is sparse [63]. Moreover, the results from the simulations are attainable without specialized hardware.

For scales larger than the models evaluated in Chapter 2, a different approach was necessary with today's (2023) off-the-shelves computers. In Chapter 3 a mathematical framework was presented to develop numerical methods for problems similar to the paperboard model.

Based on the theoretical foundation, Chapter 4 presents a multi-scale approach based on the LOD method. In this approach, representative local representations of the network model are constructed, and an accurate approximation of the entire problem is found by solving a reduced problem based on the representations. This framework is also numerically validated for paper models presented in **Paper B**. Moreover, the theory for a time-dependent wave problem was presented along with numerical experiments.

An iterative PCG method is presented in Chapter 5 based on domain decomposition. This method reduces the memory requirements compared to a direct linear solver by splitting the network into parts and solving smaller linear systems iteratively. This method enabled simulations of 400 g/m^2 paperboard models that were deemed too large for today's (2023) consumer hardware.

Future work

This thesis evaluated a linear approach to simulating paper. It would be interesting to see how the linear models compare to time-dependent and non-linear models. Stiffer results are expected for the tensile stiffness simulations, however, with the variance in the fiber parameters, the added complexity might not be necessary. Moreover, a model comparison between the Euler-Bernoulli and Timoshenko beam models might give insights into the added numerical complexity when adding the rotational components.

From the convergence analysis in **Paper F**, it is clear that the method converges fairly quickly for good initial guesses. The strength simulations in

Paper B are quite rudimentary compared to other approaches in literature [29]–[32] with more advanced fracture models. The iterative method proposed in **Paper C** could enable efficient time-dependent/non-linear simulations where small changes between iterates could be used to produce accurate initial guesses for the method. In particular, it would be interesting to see if the iterative method is efficient for geometrically exact Simo-Reissner beams [64], [65].

Non-linear simulations, such as creasing and out-of-plan strength [66] of paperboard [67], [68], on the entire micro-structure might be possible on small scales with a direct approach. For this, properties such as the shearing of the paperboard would need to be representative. For shearing to be representative, the fiber structure throughout the thickness of the model has to be representative. This could be resolved with CFD simulations of paper forming [26] or by placing the fibers in the domain and simulating the compaction process [27].

This thesis presents a mathematical foundation that can be further utilized to develop numerical methods for network-based models. Composite structures, such as reinforced composites, would be an interesting application. In [58], [69], an iterative method for solving two-dimensional elliptic problems on a continuum reinforced by a network was solved based on the assumptions in **Paper C**. Taking this further, methods could be developed for fiber-reinforced materials. Other coarsening strategies in the multiscale method have been evaluated for the network setting in [70]. Moreover, creating an algebraic coarsening strategy might be possible based on the network structure.

Assuming the network model is periodic at some scale, the LOD method presented in **Paper D** can resolve the entire micro-scale in only one period. The computational complexity would be based on that one period. With this framework, linear models on the scale of A4 sheets that consider each individual fiber might be possible. For non-linear models, where the non-linearity can be localized, the LOD method could resolve the linear domains efficiently with the non-linear parts being resolved with a direct approach or the domain decomposition method in **Paper C**.

CHAPTER 7

Summary of included papers

Paper A

***Morgan Görtz**, Gustav Kettil, Axel Målqvist, Andreas Mark, Fredrik Edelvik, A numerical multiscale method for fiber networks, Published in WCCM-ECCOMAS 2020 preceedings*

The article summarizes the initial numerical validations of the LOD method on discrete fiber-based network models. The results are an extension of the results presented in [47], showing that the LOD method is capable of upscaling less structured networks. These initial numerical results motivated us to continue the theoretical development of the LOD method's use on general network problems.

Paper B

***Morgan Görtz**, Gustav Kettil, Axel Målqvist, Mats Fredlund, Kenneth Wester, Fredrik Edelvik, Network models for predicting structural properties of paper, Nordic Pulp & Paper Research Journal, vol. 37, no. 4, 2022, pp. 712-724*

In this article, one of the paper network models presented in Chapter 2 is presented, analyzed, and validated. First, the network model parameters are methodically defined either with experimental data or using published values in the literature. The discretization parameters of the model are then analyzed and motivated. Tensile stiffness, tensile strength, and bending resistance experiments are simulated and validated against experimental data in cross- and machine directions. The simulation domains chosen are motivated by domain studies, showing that the forces scale appropriately for different domain sizes. The validation results show that the paper network model can simulate the mentioned structural experiments accurately. Moreover, the simulations are fast, with the simulations only taking a couple of minutes on consumer-grade hardware.

Paper C

***Morgan Görtz**, Fredrik Hellman, Axel Målqvist, Iterative solution of spatial network models by subspace decomposition, Mathematics of Computation, Vol. 93, 2024, pp. 233–258*

This article presents the mathematical framework enabling continuum-like analysis on network models presented in Chapter 3, as well as formulating the assumptions on the network structure. This framework is then used to prove the convergence of the preconditioned CG method presented in Chapter 5 on elliptic network problems.

Paper D

*Fredrik Edelvik, **Morgan Görtz**, Fredrik Hellman, Gustav Kettil, Axel Målqvist, Numerical homogenization of spatial network models, Computer Methods in Applied Mechanics and Engineering, Vol 418, Part B, 2024, 11659*

This article presents the mathematical foundation used to prove an a priori error bound for the LOD method on general network problems. The theoretical results build on the assumptions presented in **Paper C**, where the assumptions make it possible to construct an artificial uniform coarse grid and an effective interpolation operator for the LOD method. The main result of this paper is a proven a priori error bound for LOD approximations and numerically validated for the model presented in **Paper B**.

Paper E

***Morgan Görtz**, Per Ljung, Axel Målqvist, Multiscale methods for solving wave equations on spatial networks, Computer Methods in Applied Mechanics and Engineering, Vol. 410, 2023, 116008*

In this work, the theory for the LOD method applied to network problems presented in **Paper D** is extended for wave propagation problems. This is performed by combining the developed theory in **Paper D** with an energy-conserving temporal scheme. With well-prepared initial data, it was possible to derive an a priori error bound of optimal order with respect to the space and time discretization. The theoretical results were evaluated numerically both for heat, and the structural model used in **Paper B**.

Paper F

***Morgan Görtz**, Gustav Kettil, Axel Målqvist, Mats Fredlund, Fredrik Edelvik, Iterative method for large-scale Timoshenko beam models, assessed on commercial-grade paperboard, Submitted*

This article is the continuation of **Paper B**, where structural properties of industrial-grade paperboard are simulated. Here a Timoshenko beam model is used, and tensile stiffness and bending resistance are evaluated for various three-ply paperboards comprised of different types of pulp. The results illustrate the limit of commercial linear solvers for these types of micro-mechanical models. Moreover, the iterative method presented in **Paper C** is used to solve problems four times larger than the mentioned limit. From these results, it is clear that it is possible to do these types of micro-mechanical simulations on consumer hardware and that this approach might serve as a useful tool in the industry.

References

[1] D. D. Furszyfer Del Rio, B. K. Sovacool, S. Griffiths, *et al.*, "Decarbonizing the pulp and paper industry: A critical and systematic review of sociotechnical developments and policy options," *Renewable and Sustainable Energy Reviews*, vol. 167, 2022.

[2] G. Pettersson, S. Norgren, P. Engstrand, M. Rundlöf, and H. Höglund, "Aspects on bond strength in sheet structures from tmp and ctmp – a review," *Nordic Pulp and Paper Research Journal*, vol. 36, no. 2, pp. 177–213, 2021.

[3] U. Hirn and R. Schennach, "Comprehensive analysis of individual pulp fiber bonds quantifies the mechanisms of fiber bonding in paper," *Scientific Reports*, vol. 5, 2015, Cited by: 96; All Open Access, Gold Open Access, Green Open Access.

[4] L. Orgéas, P. Dumont, F. Martoïa, C. Marulier, S. Le Corre, and D. Caillerie, "On the role of fibre bonds on the elasticity of low-density papers: A micro-mechanical approach," *Cellulose*, vol. 28, no. 15, pp. 9919–9941, 2021.

[5] H. Cox, "The elasticity and strength of paper and other fibrous materials," *British Journal of Applied Physics*, vol. 3, no. 3, pp. 72–79, 1952.

[6] D. Page, "A theory for the tensile strength of paper," *Tappi Journal*, vol. 17, no. 10, pp. 583–681, 2018.

[7] R. W. Perkins and R. E. Mark, "On the structural theory of the elastic behavior of paper.," *TAPPI*, vol. 59, no. 12, pp. 118–120, 1976.

[8] M. Rigdahl, H. Andersson, B. Westerlind, and H. Hollmark, "Elastic behaviour of low density paper described by network mechanics," *Fibre Science and Technology*, vol. 19, no. 2, pp. 127–144, 1983.

[9] E. Borgqvist, M. Wallin, M. Ristinmaa, and J. Tryding, "An anisotropic in-plane and out-of-plane elasto-plastic continuum model for paperboard," *Composite Structures*, vol. 126, pp. 184–195, 2015.

[10] G. Lindberg and A. Kulachenko, "Tray forming operation of paperboard: A case study using implicit finite element analysis," *Packaging Technology and Science*, vol. 35, no. 2, pp. 183–198, 2022.

[11] K. Robertsson, M. Wallin, E. Borgqvist, M. Ristinmaa, and J. Tryding, "A rate-dependent continuum model for rapid converting of paperboard," *Applied Mathematical Modelling*, vol. 99, pp. 497–513, 2021.

[12] A. El Moumen, T. Kanit, and A. Imad, "Numerical evaluation of the representative volume element for random composites," *European Journal of Mechanics, A/Solids*, vol. 86, 2021.

[13] A. Shahsavari and R. Picu, "Size effect on mechanical behavior of random fiber networks," *International Journal of Solids and Structures*, vol. 50, no. 20-21, pp. 3332–3338, 2013.

[14] J. E. Bishop, J. M. Emery, R. V. Field, C. R. Weinberger, and D. J. Littlewood, "Direct numerical simulations in solid mechanics for understanding the macroscale effects of microscale material variability," *Computer Methods in Applied Mechanics and Engineering*, vol. 287, pp. 262–289, 2015.

[15] R. Mansour and A. Kulachenko, "4 - stochastic constitutive model of thin fibre networks," in *Mechanics of Fibrous Networks*, ser. Elsevier Series in Mechanics of Advanced Materials, V. V. Silberschmidt, Ed., Elsevier, 2022, pp. 75–112, ISBN: 978-0-12-822207-2.

[16] R. Horn, "Morphology of wood pulp fiber from softwoods and influence on paper strength," US For Prod Lab Res Pap, Tech. Rep., 1974.

[17] G. Wang, S. Q. Shi, J. Wang, Y. Yu, S. Cao, and H. Cheng, "Tensile properties of four types of individual cellulosic fibers," *Wood and Fiber Science*, vol. 43, no. 4, pp. 353–364, 2011.

[18] M. Dauer, A. Wolfbauer, T. Seidlhofer, and U. Hirn, "Shear modulus of single wood pulp fibers from torsion tests," *Cellulose*, vol. 28, no. 12, pp. 8043–8054, 2021.

[19] C. Czibula, T. Seidlhofer, C. Ganser, U. Hirn, and C. Teichert, "Longitudinal and transverse low frequency viscoelastic characterization of wood pulp fibers at different relative humidity," *Materialia*, vol. 16, 2021.

[20] M. Hubbe, "Bonding between cellulosic fibers in the absence and presence of dry-strength agents - a review," *BioResources*, vol. 1, Nov. 2006.

[21] B. N. J. Persson, C. Ganser, F. Schmied, *et al.*, "Adhesion of cellulose fibers in paper," *Journal of Physics Condensed Matter*, vol. 25, no. 4, 2013.

[22] R. C. Hamlen, "Paper structure, mechanics, and permeability: Computer-aided modeling," Ph.D. dissertation, University of Minnesota, 1991.

[23] V. Räisänen, M. Alava, R. Nieminen, and K. Niskanen, "Elastic-plastic behaviour in fibre networks," *Nordic Pulp and Paper Research Journal*, vol. 11, no. 4, pp. 243–248, 1996.

[24] S. Heyden, "Network modelling for evaluation of mechanical properties of cellulose fibre fluff," Ph.D. dissertation, LTH, 2000.

[25] A. Kulachenko and T. Uesaka, "Direct simulations of fiber network deformation and failure," *Mechanics of Materials*, vol. 51, pp. 1–14, 2012.

[26] E. Svenning, A. Mark, F. Edelvik, *et al.*, "Multiphase simulation of fiber suspension flows using immersed boundary methods," *Nordic Pulp and Paper Research Journal*, vol. 27, no. 2, pp. 184–191, 2012.

[27] C. Ceccato, A. Brandberg, A. Kulachenko, and C. Barbier, "Micromechanical modeling of the paper compaction process," *Acta Mechanica*, vol. 232, no. 9, pp. 3701–3722, 2021.

[28] G. Kettil, "Multiscale methods for simulation of paper making," Ph.D. dissertation, Chalmers University of Technology and University of Gothenburg, 2019.

[29] S. Borodulina, A. Kulachenko, S. Galland, and M. Nygårds, "Stress-strain curve of paper revisited," *Nordic Pulp and Paper Research Journal*, vol. 27, no. 2, pp. 318–328, 2012.

[30] V. Tojaga, A. Kulachenko, S. Östlund, and T. C. Gasser, "Modeling multi-fracturing fibers in fiber networks using elastoplastic timoshenko beam finite elements with embedded strong discontinuities — formulation and staggered algorithm," *Computer Methods in Applied Mechanics and Engineering*, vol. 384, 2021.

[31] V. Tojaga, A. Prapavesis, J. Faleskog, T. C. Gasser, A. W. van Vuure, and S. Östlund, "Continuum damage micromechanics description of the compressive failure mechanisms in sustainable biocomposites and experimental validation," *Journal of the Mechanics and Physics of Solids*, vol. 171, 2023.

[32] L. Varandas, G. Catalanotti, A. Melro, R. Tavares, and B. Falzon, "Micromechanical modelling of the longitudinal compressive and tensile failure of unidirectional composites: The effect of fibre misalignment introduced via a stochastic process," *International Journal of Solids and Structures*, vol. 203, pp. 157–176, 2020.

[33] S. Adriaenssens and M. Barnes, "Tensegrity spline beam and grid shell structures," *Engineering Structures*, vol. 23, no. 1, pp. 29–36, 2001.

[34] J. Chu, B. Engquist, M. Prodanović, and R. Tsai, "A multiscale method coupling network and continuum models in porous media i: Steady-state single phase flow," *Multiscale Modeling and Simulation*, vol. 10, no. 2, pp. 515–549, 2012.

[35] W.-L. Jin, "A kinematic wave theory of multi-commodity network traffic flow," *Transportation Research Part B: Methodological*, vol. 46, no. 8, pp. 1000–1022, 2012.

[36] R. Ewing, O. Iliev, R. Lazarov, I. Rybak, and J. Willems, "A simplified method for upscaling composite materials with high contrast of the conductivity," *SIAM Journal on Scientific Computing*, vol. 31, no. 4, pp. 2568–2586, 2009.

[37] A. Brandt, "Multi-level adaptive solutions to boundary-value problems," *Mathematics of Computation*, vol. 31, no. 138, pp. 333–390, 1977.

[38] R. Kornhuber and H. Yserentant, "Numerical homogenization of elliptic multiscale problems by subspace decomposition," *Multiscale Modeling and Simulation*, vol. 14, no. 3, pp. 1017–1036, 2016.

[39] J. Xu and L. Zikatanov, "Algebraic multigrid methods," *Acta Numerica*, vol. 26, pp. 591–721, 2017.

[40] Y. Efendiev, J. Galvis, and T. Y. Hou, "Generalized multiscale finite element methods (gmsfem)," *Journal of Computational Physics*, vol. 251, pp. 116–135, 2013, ISSN: 0021-9991.

[41] W. E and B. Engquist, "The Heterognous Multiscale Methods," *Communications in Mathematical Sciences*, vol. 1, no. 1, pp. 87–132, 2003.

[42] A. Målqvist and D. Peterseim, "Localization of elliptic multiscale problems," *Mathematics of Computation*, vol. 83, no. 290, pp. 2583–2603, 2014.

[43] R. Cook, D. Malkus, M. Plesha, and R. Witt, "Concepts and applications of finite element analysis, 4th edition," in New York: Wiley, 2002, pp. 10–13.

[44] M. Görtz, "Experimental validation and numerical upscaling of linear network models for simulation of pape," Licentiate of philosophy, Chalmers University of Technology, 2022.

[45] L. A. Carlsson and C. N. Fellers, "Flexural stiffness of multi-ply paperboard," *Fibre Science and Technology*, vol. 13, no. 3, pp. 213–223, 1980.

[46] H. Hollmark, R. W. Perkins, and H. Andersson, "Mechanical properties of low density sheets.," *TAPPI*, vol. 61, no. 9, pp. 69–72, 1978.

[47] G. Kettil, A. Målqvist, A. Mark, M. Fredlund, K. Wester, and F. Edelvik, "Numerical upscaling of discrete network models," *BIT Numerical Mathematics*, vol. 60, no. 1, pp. 67–92, 2020.

[48] R. E. Mark, C. Habeger, J. Borch, and M. B. Lyne, "Handbook of physical testing of paper (vol. 1). second edition," in New York: Dekker, 2002, pp. 233–256.

[49] Q. S. Xia, M. C. Boyce, and D. M. Parks, "A constitutive model for the anisotropic elastic-plastic deformation of paper and paperboard," *International Journal of Solids and Structures*, vol. 39, no. 15, pp. 4053–4071, 2002.

[50] G. Marin, P. Srinivasa, M. Nygårds, and S. Östlund, "Experimental and finite element simulated box compression tests on paperboard packages at different moisture levels," *Packaging Technology and Science*, vol. 34, no. 4, pp. 229–243, 2021.

[51] M. Fiedler, "Algebraic connectivity of graphs," *Czechoslovak Mathematical Journal*, vol. 23, pp. 298–305, 1973.

[52] L. R. Scott and S. Zhang, "Finite element interpolation of nonsmooth functions satisfying boundary conditions," *Mathematics of Computation*, vol. 54, no. 190, pp. 483–493, 1990.

[53] P. Clement, "Approximation by finite element functions using local regularization.," *Rev Fr Autom Inf Rech Oper*, vol. 9, no. R-2, pp. 77–84, 1975.

[54] A. Målqvist, *Numerical homogenization by localized orthogonal decomposition*. SIAM Spotlights, 2020.

[55] "The variational multiscale method—a paradigm for computational mechanics," *Computer Methods in Applied Mechanics and Engineering*, vol. 166, no. 1, pp. 3–24, 1998.

[56] M. G. Larson and A. Målqvist, "Adaptive variational multiscale methods based on a posteriori error estimation: Energy norm estimates for elliptic problems," *Computer Methods in Applied Mechanics and Engineering*, vol. 196, no. 21, pp. 2313–2324, 2007.

[57] F. Hellman and A. Målqvist, "Contrast independent localization of multiscale problems," *Multiscale Modeling & Simulation*, vol. 15, no. 4, pp. 1325–1355, 2017.

[58] F. Hellman, A. Målqvist, and M. Mosquera, "Well-posedness and finite element approximation of mixed dimensional partial differential equations," *to appear in BIT (2024)*,

[59] P. L. A. Lang and A. Målqvist, "Localized orthogonal decomposition for a multiscale parabolic stochastic partial differential equation," *to appear in Multiscale Modeling and Simulation*, 2024.

[60] C. Engwer, P. Henning, A. Målqvist, and D. Peterseim, *Efficient implementation of the localized orthogonal decomposition method*, 2019.

[61] S. Larsson and V. Thomée, *Partial Differential Equations with Numerical Methods*. Springer, 2003.

[62] Y. Saad, *Iterative methods for sparse linear systems*, 2nd ed. SIAM, 2003.

[63] J.-W. Simon, "A review of recent trends and challenges in computational modeling of paper and paperboard at different scales," *Archives of Computational Methods in Engineering*, vol. 28, no. 4, pp. 2409–2428, 2021.

[64] J. Simo, "A finite strain beam formulation. the three-dimensional dynamic problem. part i," *Computer Methods in Applied Mechanics and Engineering*, vol. 49, no. 1, pp. 55–70, 1985.

[65] E. Reissner, "On finite deformations of space-curved beams," *Z. angew. Math. Phys.*, vol. 32, pp. 734–744, 1981.

[66] K. Robertsson, J. Engqvist, M. Wallin, M. Ristinmaa, J. Tryding, and E. Borgqvist, "Out-of-plane uniaxial loading of paperboard: Experimental procedure and evaluation," *Nordic Pulp and Paper Research Journal*, 2023.

[67] "Experimental and numerical studies of creasing of paperboard," *International Journal of Solids and Structures*, vol. 46, no. 11, pp. 2493–2505, 2009, ISSN: 0020-7683.

[68] K. Robertsson, E. Jacobsson, M. Wallin, E. Borgqvist, M. Ristinmaa, and J. Tryding, "A continuum damage model for creasing and folding of paperboard," *Packaging Technology and Science*, vol. 36, no. 12, pp. 1037–1050, 2023.

[69] M. Mosquera, "Numerical approximation of mixed dimensional partial differential equations," Licentiate of philosophy, Chalmers University of Technology and University of Gothenburg, 2013.

[70] M. Hauck and A. Målqvist, *Super-localization of spatial network models*, 2022.